

Higgs boson precision analysis of two-Higgs-doublet models: Full LHC Run 1 and Run 2 data

Yongtae Heo,^{a,d} Jae Sik Lee,^b and Chan Beom Park^{c,d}

Department of Physics & IUEP, Chonnam National University, Gwangju 61186, Korea

(Dated: April 23, 2025)

We present the results obtained by performing global fits of two-Higgs-doublet models (2HDMs) using the full Run 1 and Run 2 Higgs datasets collected at the LHC. Avoiding unwanted tree-level flavor-changing neutral currents and including the wrong-sign cases, we consider 12 scenarios across six types of 2HDMs: Inert, type I, type II, type III, type IV, and Aligned 2HDMs. Our main results are presented in Table III and Fig. 1. We find that the type-I 2HDM provides the best fit, while the wrong-sign scenarios of the type-II and type-IV 2HDMs, where the normalized Yukawa coupling to down-type quarks is opposite in sign to the Standard Model (SM), are disfavored. We also observe that the Aligned 2HDM gives the second-best fit when the Yukawa couplings to down-type quarks take the same sign as in the SM, regardless of the sign of the Yukawa couplings to the charged leptons.

arXiv:2502.02992v2 [hep-ph] 23 Apr 2025

^aContact author: yongtae1heo@gmail.com

^bContact author: jslee@jnu.ac.kr

^cContact author: cbpark@jnu.ac.kr

^dThese authors contributed equally to this work.

I. INTRODUCTION

Since the ATLAS and CMS collaborations independently reported the observation of a new scalar particle in the search for the Standard Model (SM) Higgs boson in 2012 [1, 2], its properties and couplings to SM particles have been extensively investigated. At the LHC, the 125 GeV Higgs boson has been observed through six production processes and via seven decay modes [3, 4]. For the Higgs production processes, investigated are the two main production processes of gluon-gluon fusion (ggF) and vector-boson fusion (VBF), along with four subleading ones in which the produced Higgs boson is associated with a $V = W/Z$ boson (WH/ZH), a top-quark pair (ttH), or a single top quark (tH). Through its seven decay modes into $b\bar{b}$, WW^* , $\tau^+\tau^-$, ZZ^* , $\gamma\gamma$, $Z\gamma$, and $\mu^+\mu^-$, the couplings to the two massive vector bosons are well measured with a few percent accuracy. Third-generation Yukawa couplings are firmly established, and the decays into a pair of muons and $Z\gamma$ are now emerging.

Recently, we showed that the full LHC Higgs precision data are no longer best described by the SM Higgs boson [5]. The best-fitted values of the normalized Yukawa couplings are about 2σ below their corresponding SM values, with 1σ errors of 3%–5% in a model-independent way. While the deviation of the normalized Yukawa couplings has been noticed previously in Refs. [3, 4, 6] especially when they are universal, our comprehensive analysis strengthens and confirms this observation by combining the ATLAS and CMS Run 2 datasets [3, 4].¹

In this work, we perform global fits of two-Higgs-doublet models (2HDMs) without tree-level Higgs-mediated flavor-changing neutral current (FCNC). The 2HDM models, in which the SM is extended by adding one more Higgs doublet, provide one of the most favored and well-motivated frameworks beyond the SM [8]. Noting that the Aligned 2HDM [9] could accommodate frequently referred 2HDMs without FCNC on the market by appropriately choosing the model parameters, we consider six types of CP-conserving 2HDMs in this work, as summarized in Table I.

This paper is organized as follows. Section II reviews the Higgs potential of 2HDMs in the Higgs basis and the 125 GeV Higgs couplings to SM particles under the assumption that the lighter CP-even neutral state plays the role of the SM Higgs boson. In Sec. III, we present the main results of our analysis, and a detailed discussion of some representative 2HDM scenarios is given in Sec. IV. Conclusions are drawn in Sec. V. In Appendix A, we deliver additional details of the 2HDM scenarios not covered in Sec. IV. Appendix B shows the correlations among the 125 GeV Higgs boson couplings to SM particles. Finally, Appendix C includes the fitting results obtained by imposing constraints from the perturbativity of top-quark Yukawa coupling, the radiative $b \rightarrow s\gamma$ decay, the primary theoretical conditions on the Higgs potential, and the electroweak precision observables.

II. FRAMEWORK

In the so-called Higgs basis [12, 13] where only one doublet contains a nonvanishing vacuum expectation value v , the general 2HDM scalar potential can be expressed as [11]

$$\begin{aligned} V_{\mathcal{H}} = & Y_1(\mathcal{H}_1^\dagger \mathcal{H}_1) + Y_2(\mathcal{H}_2^\dagger \mathcal{H}_2) + Y_3(\mathcal{H}_1^\dagger \mathcal{H}_2) + Y_3^*(\mathcal{H}_2^\dagger \mathcal{H}_1) \\ & + Z_1(\mathcal{H}_1^\dagger \mathcal{H}_1)^2 + Z_2(\mathcal{H}_2^\dagger \mathcal{H}_2)^2 + Z_3(\mathcal{H}_1^\dagger \mathcal{H}_1)(\mathcal{H}_2^\dagger \mathcal{H}_2) + Z_4(\mathcal{H}_1^\dagger \mathcal{H}_2)(\mathcal{H}_2^\dagger \mathcal{H}_1) \\ & + Z_5(\mathcal{H}_1^\dagger \mathcal{H}_2)^2 + Z_5^*(\mathcal{H}_2^\dagger \mathcal{H}_1)^2 + Z_6(\mathcal{H}_1^\dagger \mathcal{H}_1)(\mathcal{H}_1^\dagger \mathcal{H}_2) + Z_6^*(\mathcal{H}_1^\dagger \mathcal{H}_1)(\mathcal{H}_2^\dagger \mathcal{H}_1) \\ & + Z_7(\mathcal{H}_2^\dagger \mathcal{H}_2)(\mathcal{H}_1^\dagger \mathcal{H}_2) + Z_7^*(\mathcal{H}_2^\dagger \mathcal{H}_2)(\mathcal{H}_2^\dagger \mathcal{H}_1), \end{aligned} \quad (1)$$

which contains three dimensionful quadratic and seven dimensionless quartic parameters, four of which are complex. In this work, we consider the CP-conserving case, assuming that $\Im(Y_3) = \Im(Z_{5,6,7}) = 0$. The complex $SU(2)_L$ doublets of \mathcal{H}_1 and \mathcal{H}_2 can be parametrized as

$$\mathcal{H}_1 = \begin{pmatrix} G^+ \\ \frac{1}{\sqrt{2}}(v + \varphi_1 + iG^0) \end{pmatrix}; \quad \mathcal{H}_2 = \begin{pmatrix} H^+ \\ \frac{1}{\sqrt{2}}(\varphi_2 + iA) \end{pmatrix}, \quad (2)$$

where $v = (\sqrt{2}G_F)^{-1/2} \simeq 246.22$ GeV, and $G^{\pm,0}$ and H^\pm stand for the Goldstone and charged Higgs bosons, respectively. For the neutral Higgs bosons, A denotes a CP-odd mass eigenstate and the two states φ_1 and φ_2 mix to form two CP-even mass eigenstates, one of which should correspond to the SM Higgs boson. To describe the mixing between the two

¹The Run 1 dataset [7] is also included.

TABLE I. The alignment parameters of the 2HDMs considered in this work. For the four (I, II, III, IV) types of 2HDM based on the Glashow-Weinberg condition [10], we follow the conventions found in, for example, Ref. [11].

	Inert	I	II	III	IV	Aligned
ζ_u	0	$1/t_\beta$	$1/t_\beta$	$1/t_\beta$	$1/t_\beta$	ζ_u
ζ_d	0	$1/t_\beta$	$-t_\beta$	$1/t_\beta$	$-t_\beta$	ζ_d
ζ_ℓ	0	$1/t_\beta$	$-t_\beta$	$-t_\beta$	$1/t_\beta$	ζ_ℓ
		$\zeta_d = \zeta_\ell = \zeta_u$	$\zeta_d = \zeta_\ell = -1/\zeta_u$	$\zeta_d = -1/\zeta_\ell = \zeta_u$	$\zeta_d = -1/\zeta_\ell = -1/\zeta_u$	all independent

CP-even states φ_1 and φ_2 , we introduce the mixing angle γ as follows:²

$$\begin{pmatrix} \varphi_1 \\ \varphi_2 \end{pmatrix} = \begin{pmatrix} c_\gamma & s_\gamma \\ -s_\gamma & c_\gamma \end{pmatrix} \begin{pmatrix} h \\ H \end{pmatrix}, \quad (3)$$

assuming that h is the lightest neutral Higgs boson with $M_h \simeq 125$ GeV. Then, in terms of the four masses M_{h,H,A,H^\pm} and the mixing angle γ , the quartic couplings $\{Z_1, Z_4, Z_5, Z_6\}$ are given by

$$\begin{aligned} Z_1 &= \frac{1}{2v^2} (c_\gamma^2 M_h^2 + s_\gamma^2 M_H^2), & Z_4 &= \frac{1}{v^2} (s_\gamma^2 M_h^2 + c_\gamma^2 M_H^2 + M_A^2 - 2M_{H^\pm}^2), \\ Z_5 &= \frac{1}{2v^2} (s_\gamma^2 M_h^2 + c_\gamma^2 M_H^2 - M_A^2), & Z_6 &= \frac{1}{v^2} (-M_h^2 + M_H^2) c_\gamma s_\gamma. \end{aligned} \quad (4)$$

To summarize, the CP-conserving 2HDM scalar potential is fully specified by fixing the 9 elements of the following input-parameter set

$$\mathcal{I}^{V\mathcal{H}} = \{v, M_h; \gamma, M_H, M_A, M_{H^\pm}; Z_2, Z_3, Z_7\}, \quad (5)$$

taking account of the tadpole conditions of $Y_1 + Z_1 v^2 = 0$ and $Y_3 + Z_6 v^2/2 = 0$, and using the relation $Y_2 = M_{H^\pm}^2 - Z_3 v^2/2$.

To perform global fits to the full Higgs datasets collected at the LHC and Tevatron, we adopt the conventions and notations of the h couplings to SM particles following Ref. [14]. The Yukawa couplings of h are given by:

$$\mathcal{L}_{h\bar{f}f} = - \sum_{f=\{u,d,\ell\}} g_{h\bar{f}f}^S \frac{m_f}{v} (\bar{f}f) h, \quad (6)$$

where $\{u,d,\ell\}$ collectively represents the up-type quarks, down-type quarks, and charged leptons. The normalized coupling to the scalar fermion bilinear $\bar{f}f$ is given by:

$$g_{h\bar{f}f}^S = c_\gamma - \zeta_f s_\gamma. \quad (7)$$

Note that we have introduced three alignment parameters $\zeta_{u,d,\ell}$ as in the Aligned 2HDM [9], recognizing that all the 2HDMs considered in this work can be accommodated by appropriately choosing the three align parameters, as detailed in Table I. Additionally, we assume $\zeta_u > 0$ without loss of generality, exploiting the rephasing invariance of the Higgs potential and the Yukawa interactions [11]. The couplings of h to the massive vector bosons are described by:

$$\mathcal{L}_{hVV} = g M_W \left(g_{hWW} W_\mu^+ W^{-\mu} + g_{hZZ} \frac{1}{2c_W^2} Z_\mu Z^\mu \right) h, \quad (8)$$

with

$$g_{hWW} = g_{hZZ} \equiv g_{hVV} = c_\gamma. \quad (9)$$

²In the SM limit, where $s_\gamma \rightarrow 0$, $h = \varphi_1$ plays the role of the SM Higgs boson.

For the loop-induced h couplings to gg , $\gamma\gamma$, and $Z\gamma$, taking $M_h = 125$ GeV, we have [5]³

$$\begin{aligned} S^g &= 0.688 g_{h\bar{t}t}^S + (-0.043 + 0.063 i) g_{h\bar{b}b}^S + (-0.009 + 0.008 i) g_{h\bar{c}c}^S, \\ S^\gamma &= -8.324 g_{hWW} + 1.826 g_{h\bar{t}t}^S + (-0.020 + 0.025 i) g_{h\bar{b}b}^S + (-0.024 + 0.022 i) g_{h\bar{\tau}\tau}^S + \Delta S^\gamma, \\ S^{Z\gamma} &= -12.3401 g_{hWW} + 0.6891 g_{h\bar{t}t}^S + (-0.0186 + 0.0111 i) g_{h\bar{b}b}^S + (-0.0005 + 0.0002 i) g_{h\bar{\tau}\tau}^S + \Delta S^{Z\gamma}, \end{aligned} \quad (10)$$

with

$$\Delta S^\gamma = +g_{hH^+H^-} \frac{v^2}{2M_{H^\pm}^2} F_0(\tau_{hH^\pm}), \quad \Delta S^{Z\gamma} = +2 \frac{g_{hH^+H^-}}{c_W s_W} \frac{v^2}{M_{H^\pm}^2} I_1(\tau_{hH^\pm}, \lambda_{H^\pm}), \quad (11)$$

where $\tau_{hH^\pm} = M_h^2/4M_{H^\pm}^2$, $\lambda_{H^\pm} = M_Z^2/4M_{H^\pm}^2$, and

$$g_{hH^+H^-} = c_\gamma Z_3 - s_\gamma Z_7. \quad (12)$$

When $M_{H^\pm} \gg M_{h,Z}$, we find

$$\frac{\Delta S^{Z\gamma}(H^\pm)}{\Delta S^\gamma(H^\pm)} \simeq \frac{4}{c_W s_W} \frac{I_1(0,0)}{F_0(0)} = \frac{4}{c_W s_W} \frac{1/6}{1/3} \simeq 4.8, \quad (13)$$

and

$$\Delta S^\gamma(H^\pm) \simeq \frac{1}{6} \left[g_{hH^+H^-} \left(\frac{v}{M_{H^\pm}} \right)^2 \right]. \quad (14)$$

Note that the form factors ΔS^γ and $\Delta S^{Z\gamma}$ are strongly correlated in 2HDMs. This is contrasted to the model-independent approach taken in Ref. [5], where they are completely independent. To summarize, the h couplings to SM particles are fully specified by fixing the 5 elements of the following input-parameter set:

$$\mathcal{I}^{\text{Couplings}} = \{\zeta_u, \zeta_d, \zeta_\ell; g_{hH^+H^-}, M_{H^\pm}\}, \quad (15)$$

in addition to the mixing angle γ appearing in the Higgs potential parameter set $\mathcal{I}^{V\mathcal{H}}$.

For our numerical analysis, we adopt the basis in which $\zeta_u \geq 0$ and organize the input parameters for the Higgs potential and the h couplings as follows:

$$\mathcal{I}^{V\mathcal{H}} \oplus \mathcal{I}^{\text{Couplings}} = \left\{ v, M_h \right\}_2 \oplus \left\{ \gamma, M_{H^\pm}, g_{hH^+H^-}; \zeta_u, \zeta_d, \zeta_\ell \right\}_{3,4,6} \oplus \left\{ M_H, M_A, Z_2, Z_7 \right\}_4, \quad (16)$$

with $Z_3 = (g_{hH^+H^-} + s_\gamma Z_7)/c_\gamma$. The middle set, which contains 3 (Inert), 4 (I, II, III, IV), or 6 (Aligned) free parameters, is directly relevant for our Higgs boson precision analysis of 2HDMs. As in Ref. [5], depending on the 2HDM type, we use the following short notations for the h couplings in our global fits:

$$\begin{aligned} C_V &= g_{hVV}; C_u^S = g_{hu\bar{u}}^S, C_d^S = g_{hd\bar{d}}^S, C_\ell^S = g_{h\ell-\ell^+}^S \text{ (Aligned)}; C_{Vf} = g_{hVV} = g_{hu\bar{u}}^S = g_{hd\bar{d}}^S = g_{h\ell-\ell^+}^S \text{ (Inert)}; \\ C_f^S &= g_{hu\bar{u}}^S = g_{hd\bar{d}}^S = g_{h\ell-\ell^+}^S \text{ (I)}, C_{d\ell}^S = g_{hd\bar{d}}^S = g_{h\ell-\ell^+}^S \text{ (II)}, C_{ud}^S = g_{hu\bar{u}}^S = g_{hd\bar{d}}^S \text{ (III)}, C_{u\ell}^S = g_{hu\bar{u}}^S = g_{h\ell-\ell^+}^S \text{ (IV)}. \end{aligned} \quad (17)$$

III. ANALYSIS AND RESULTS

To perform global fits of the h couplings to the Tevatron and full LHC Run 1 and Run 2 Higgs datasets, we use a total of 77 experimental signal strengths: 76 of them are taken from Refs. [3, 4, 7, 15, 16] and presented in Tables I, II, III, and IV of Ref. [5] and the 77th one comes from the $h \rightarrow Z\gamma$ data, obtained from the combined ATLAS and CMS analysis [17].⁴ For the LHC Run 1 [7] and Run 2 [3, 4] datasets, we take account of correlation among the experimental signal strengths within each data set. On the other hand, we refer to Sec. III.B of Ref. [5] for the details of the theoretical signal strength calculations. These calculations assume that each theoretical signal strength is given by the product of

³For the normalizations of the form factors $S^{g,\gamma,Z\gamma}$ and their general expressions, and also for the loop functions F_0 and I_1 below, we refer to Ref. [14]. The SM values for these form factors are: $S_{\text{SM}}^g = 0.636 + 0.071 i$, $S_{\text{SM}}^\gamma = -6.542 + 0.046 i$, and $S_{\text{SM}}^{Z\gamma} = -11.6701 + 0.0114 i$.

⁴Specifically, we use $\mu^{\text{EXP}}(pp \rightarrow h \rightarrow Z\gamma) = \hat{\mu}^{\text{EXP}}(Z\gamma) = 2.2 \pm 0.7$, see Appendix E of Ref. [5].

the production and decay signal strengths: $\mu(\mathcal{P}, \mathcal{D}) \simeq \hat{\mu}(\mathcal{P}) \hat{\mu}(\mathcal{D})$. Once all the theoretical signal strengths μ_i 's associated with specific production processes and decay modes are obtained, we use the χ^2 statistic for n correlated observables:

$$\chi_n^2 = \sum_{i,j=1}^n \frac{(\mu_i - \mu_i^{\text{EXP}})}{\sigma_i^{\text{EXP}}} (\rho^{-1})_{ij} \frac{(\mu_j - \mu_j^{\text{EXP}})}{\sigma_j^{\text{EXP}}}, \quad (18)$$

where i, j index the n correlated production-times-decay modes and ρ is the $n \times n$ correlation matrix. Specifically, for the LHC Run 1, we use the correlation matrix given in Fig. 27 of Ref. [7]. For those of the LHC Run 2, see Auxiliary Fig. 14 presented in <https://doi.org/10.17182/hepdata.130266> (ATLAS) and the figure entitled “*Production times decay signal strength modifiers correlations*” provided in the website <https://dx.doi.org/10.17182/hepdata.127765> (CMS). For our chi-square analysis, we also consider the goodness of fit (gof), which quantifies the agreement with the experimentally measured signal strengths in a given fit. Note that the gof approaches 1 as the value of χ^2 per degree of freedom (dof) becomes smaller.

TABLE II. The 12 scenarios considered in our global fit to the six types of 2HDMs and the varying parameters in each scenario. Also shown are the novel combinations which are well constrained by the Higgs precision data.

Types	Scenarios	Varying Parameters	Novel Combinations Constrained
Inert	Inrt	$s_\gamma, g_{hH^+H^-}, M_{H^\pm}$	s_γ
Type I	I	$s_\gamma, t_\beta = \frac{1}{\zeta_u}, g_{hH^+H^-}, M_{H^\pm}$	$-s_\gamma/t_\beta$
Type II	II ⁺ ($C_{d\ell}^S > 0$)		$s_\gamma(t_\beta - 1/t_\beta)$
	II ⁻ ($C_{d\ell}^S < 0$)		$s_\gamma t_\beta$
Type III	III ⁺ ($C_\ell^S > 0$)		$s_\gamma(t_\beta - 1/t_\beta)$
	III ⁻ ($C_\ell^S < 0$)		$s_\gamma t_\beta$
Type IV	IV ⁺ ($C_d^S > 0$)		$-s_\gamma/t_\beta$
	IV ⁻ ($C_d^S < 0$)		$s_\gamma t_\beta$
Aligned	A ⁺⁺ ($C_d^S > 0, C_\ell^S > 0$)	$s_\gamma, \zeta_u, \zeta_d, \zeta_\ell, g_{hH^+H^-}, M_{H^\pm}$	$-s_\gamma \zeta_u, -s_\gamma \zeta_d, -s_\gamma \zeta_\ell$
	A ⁺⁻ ($C_d^S > 0, C_\ell^S < 0$)		
	A ⁻⁺ ($C_d^S < 0, C_\ell^S > 0$)		
	A ⁻⁻ ($C_d^S < 0, C_\ell^S < 0$)		

The so-called wrong-sign alignment can occur when $s_\gamma \zeta_f = 2$ with $c_\gamma \rightarrow 1$, resulting in normalized Yukawa couplings that are equal in strength but opposite in sign to the SM couplings. Since $c_\gamma = g_{hVV}$ is constrained to be (very) close to 1 by precision Higgs data, the wrong-sign alignment can occur only when $|\zeta_f| \gg 1$. In our global fits of the six types of 2HDMs, we treat the wrong-sign case as an independent scenario, as it occupies a completely different region of parameter space in the (s_γ, ζ_f) plane compared to the same-sign case, where $|s_\gamma \zeta_f|$ is small. We observe that $C_{d\ell}^S$, C_ℓ^S , and C_d^S can take the wrong signs in type II, III, and IV 2HDMs, respectively. Meanwhile, in the Aligned 2HDM, C_d^S and C_ℓ^S are independent of each other and from C_u^S . As a result, we have identified 12 distinct scenarios, as shown in Table II. In the same table, we also list the parameters to be varied in each scenario and the novel combinations which turn out to be well constrained by the Higgs precision data.

In Table III, we present our main results obtained by performing global fits of 2HDMs using the full Higgs datasets collected at the LHC and Tevatron. In Fig. 1, we compare the gof values for the 12 scenarios of six types of 2HDMs. The current Higgs precision data pull the SM gof down to 0.2424. This is basically due to the deviations of the combined signal strengths of the Higgs decay modes into $\gamma\gamma$, bb , and $\tau\tau$ from the SM: see Table VI and Sec. IV.A.2 in Ref. [5]. In **Inrt**, two degenerate minima appear depending on the sign of s_γ , although the Higgs couplings cannot distinguish the sign. We also find (almost) degenerate minima in the **II**⁺ and **III**⁺ scenarios, depending on the sign of s_γ . However, we conclude that it is not a parametric feature, but rather an accidental one since we observe that this degeneracy is lifted when turning off the correlation in the LHC datasets. Scenario **I** provides the best fit among all the 2HDMs considered in this work. In fact, all the 2HDM scenarios except **II**⁻ and **IV**⁻ yield the better gof values than the SM one. We also observe that the wrong-sign C_d^S results in worse fits in the **A**^{-±} scenario compared to **A**^{+±}. This is due to the interference between the top- and bottom-quark contributions to ggF, which leads to larger values of χ^2 when C_d^S takes the wrong sign. On the other hand, when only C_ℓ^S takes the wrong sign as in **III**⁻, **A**⁺⁻, and **A**⁻⁻, the fits are very slightly better compared to the corresponding scenarios with positive C_ℓ^S . This improvement is because the flip of sign of C_ℓ^S induces a shift in ΔS^γ , leading to a larger deviation of $\Delta S^{Z\gamma}$ from 0 which improves the fit to the $h \rightarrow Z\gamma$ data, see Eqs. (10) and (13). The preference for the wrong-sign C_ℓ^S is a new feature driven by the inclusion of the $h \rightarrow Z\gamma$ data, although it is nearly meaningless with the current statistical precision.

TABLE III. The minimal chi-square per degree of freedom (χ^2_{\min}/dof), goodness of fit (gof), 1σ confidence interval of s_γ , and the best-fitted values of the 125 GeV Higgs couplings to SM particles in the 12 scenarios considered in our global fit to the six types of 2HDMs. For the SM, we obtain $\chi^2_{\min}/\text{dof} = 85.29/77$ and $\text{gof} = 0.2424$.

		χ^2_{\min}/dof	gof	s_γ	C_V	C_f^S		ΔS^γ	$\Delta S^{Z\gamma}$	
Inrt	$s_\gamma > 0$	80.28/74	0.2889	[0, 0.25]	$C_{Vf} = 0.9872^{+0.0128}_{-0.0198}$			$-0.421^{+0.180}_{-0.200}$	$-2.100^{+0.938}_{-0.910}$	
	$s_\gamma < 0$			[-0.25, 0]						
I		75.94/73	0.3839	[0, 0.18]	$0.9999^{+0.0001}_{-0.0166}$	$0.929^{+0.033}_{-0.029}$		$-0.216^{+0.179}_{-0.200}$	$-1.036^{+0.859}_{-1.020}$	
II ⁺	$s_\gamma > 0$	79.82/73	0.2734	[0, 0.02]	$1.0_{-0.0001}$	$C_u^S = 0.971^{+0.028}_{-0.025}$	$C_{d\ell}^S = 1.0^{+0.010}_{-0.000}$	$-0.413^{+0.176}_{-0.182}$	$-1.993^{+0.853}_{-0.871}$	
	$s_\gamma < 0$	79.85/73	0.2727	[-0.02, 0]	$1.0_{-0.0001}$	$C_u^S = 1.0^{+0.008}_{-0.000}$	$C_{d\ell}^S = 0.969^{+0.031}_{-0.029}$	$-0.261^{+0.206}_{-0.193}$	$-1.254^{+0.988}_{-0.940}$	
II ⁻		86.62/73	0.1317	[-0.25, -0.02]	$0.9968^{+0.0030}_{-0.0281}$	$C_u^S = 1.0^{+0.001}_{-0.000}$	$C_{d\ell}^S = -0.993^{+0.043}_{-0.034}$	$-0.350^{+0.212}_{-0.209}$	$-1.682^{+1.018}_{-1.007}$	
III ⁺	$s_\gamma > 0$	79.11/73	0.2923	[0, 0.02]	$1.0_{-0.0003}$	$C_{ud}^S = 0.951^{+0.037}_{-0.036}$	$C_\ell^S = 1.0^{+0.010}_{-0.000}$	$-0.300^{+0.174}_{-0.180}$	$-1.443^{+0.839}_{-0.866}$	
	$s_\gamma < 0$	79.10/73	0.2923	[-0.02, 0]	$1.0_{-0.0003}$	$C_{ud}^S = 1.0^{+0.011}_{-0.000}$	$C_\ell^S = 0.950^{+0.037}_{-0.039}$	$-0.331^{+0.175}_{-0.172}$	$-1.593^{+0.843}_{-0.822}$	
III ⁻		78.96/73	0.2962	[-0.15, -0.02]	$0.9998^{+0.00002}_{-0.0110}$	$C_{ud}^S = 1.0^{+0.0003}_{-0.0000}$	$C_\ell^S = -0.951^{+0.040}_{-0.037}$	$-0.374^{+0.172}_{-0.176}$	$-1.800^{+0.831}_{-0.855}$	
IV ⁺		78.60/73	0.3062	[0, 0.02]	$1.0_{-0.0002}$	$C_{u\ell}^S = 0.968^{+0.021}_{-0.020}$	$C_d^S = 1.0^{+0.015}_{-0.000}$	$-0.397^{+0.174}_{-0.176}$	$-1.907^{+0.837}_{-0.848}$	
IV ⁻		85.55/73	0.1495	[-0.15, -0.02]	$0.9997^{+0.00005}_{-0.0110}$	$C_{u\ell}^S = 1.0^{+0.0000}_{-0.0002}$	$C_d^S = -1.035^{+0.031}_{-0.040}$	$-0.402^{+0.185}_{-0.213}$	$-1.955^{+0.909}_{-1.004}$	
						C_u^S	C_d^S	C_ℓ^S		
A ⁺⁺		75.70/71	0.3302	[0, 0.30]	$0.9970^{+0.0030}_{-0.0413}$	$0.931^{+0.036}_{-0.048}$	$0.912^{+0.048}_{-0.095}$	$0.923^{+0.039}_{-0.053}$	$-0.182^{+0.221}_{-0.213}$	$-0.875^{+1.064}_{-1.025}$
A ⁺⁻		75.52/71	0.3347	[0.02, 0.30]	$0.9918^{+0.0080}_{-0.0366}$	$0.928^{+0.038}_{-0.043}$	$0.899^{+0.060}_{-0.084}$	$-0.917^{+0.046}_{-0.044}$	$-0.219^{+0.212}_{-0.215}$	$-1.051^{+1.018}_{-1.037}$
A ⁻⁺		77.20/71	0.2873	[0.02, 0.28]	$0.9993^{+0.0005}_{-0.0391}$	$0.888^{+0.039}_{-0.037}$	$-0.910^{+0.086}_{-0.052}$	$0.930^{+0.036}_{-0.054}$	$-0.167^{+0.213}_{-0.220}$	$-0.803^{+1.023}_{-1.079}$
A ⁻⁻		77.03/71	0.2918	[0.02, 0.28]	$0.9931^{+0.0067}_{-0.0333}$	$0.888^{+0.040}_{-0.037}$	$-0.894^{+0.072}_{-0.068}$	$-0.921^{+0.044}_{-0.047}$	$-0.200^{+0.194}_{-0.230}$	$-0.961^{+0.934}_{-1.103}$

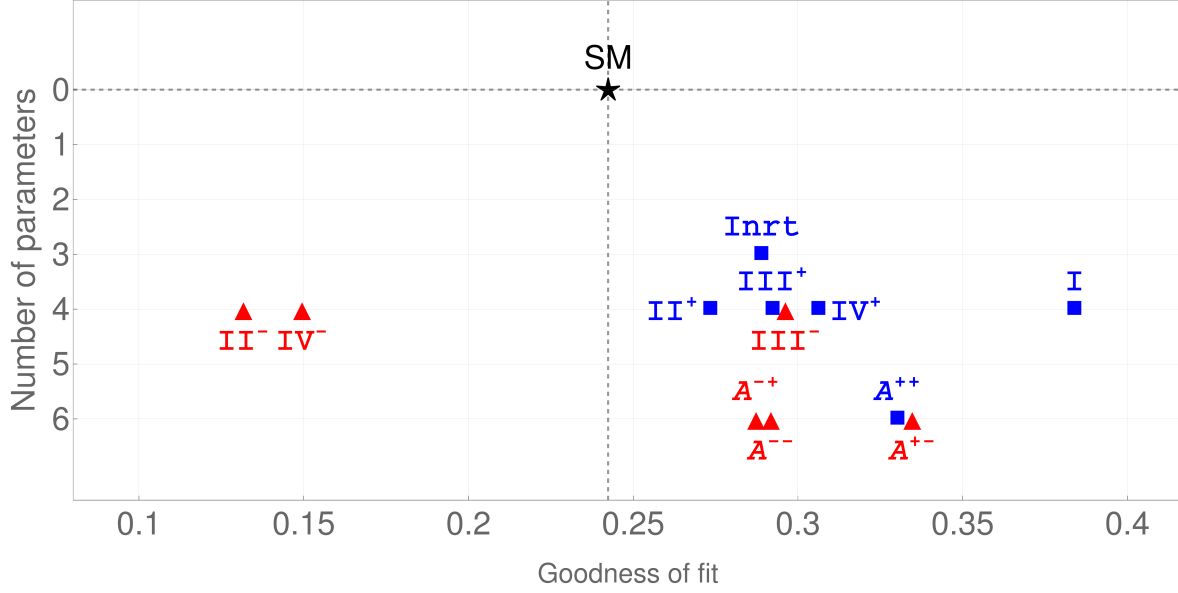


FIG. 1. Goodness of fit for the 12 scenarios considered in our global fit of the six types of 2HDMs. Blue boxes represent the scenarios in which all the Yukawa couplings are positive, while the wrong-sign scenarios are denoted by red triangles. The SM point is marked with a star.

For the couplings, our finding are as follows:

- In **Inrt**, the gauge-Higgs coupling C_V is equal to the normalized Yukawa coupling C_f^S , and C_{Vf} is consistent with the SM, with 1σ errors of 1%-2%.
- The 1σ confidence intervals (CIs) of s_γ in **II⁺**, **III⁺**, and **IV⁺** are at a few percent level. The deviation of $C_V = c_\gamma$ from 1 is extremely small, with 1σ errors of 0.01%-0.03%. In other cases, the best-fitted values of C_V are very close to 1, with 1σ errors of 1%-4%.
- In **I** for which we have obtained the best value of gof, the best-fitted value of the normalized Yukawa coupling is about 2σ below the SM value of 1, with 1σ errors of 3%.

- In the wrong-sign scenarios of \mathbf{II}^- , \mathbf{III}^- , and \mathbf{IV}^- , the best-fitted values of $C_{d\ell}^S$, C_ℓ^S and C_d^S are around -1 with 1σ errors of 4%. The best-fitted values for the other couplings, C_u^S (\mathbf{II}^-), C_{ud}^S (\mathbf{III}^-), and C_{ul}^S (\mathbf{IV}^-), are extremely close to 1, with 1σ errors of less than 0.1%.
- In \mathbf{II}^+ and \mathbf{III}^+ , each of which has two (almost) degenerate minima, the best-fitted values are: $(C_u^S, C_{d\ell}^S) \simeq (0.97, 1)$ and $(C_{ud}^S, C_\ell^S) \simeq (0.95, 1)$ when $s_\gamma > 0$ and $t_\beta \ll 1$.⁵ Conversely, when $s_\gamma < 0$ and $t_\beta \gg 1$, they become $(C_u^S, C_{d\ell}^S) \simeq (1, 0.97)$ and $(C_{ud}^S, C_\ell^S) \simeq (1, 0.95)$. In \mathbf{IV}^+ , the best-fitted values are $(C_{ul}^S, C_d^S) \simeq (0.97, 1)$. The 1σ errors are about 1% (2%–4%) when the best-fitted value is equal to (smaller than) 1.
- In each of \mathbf{II}^\pm , \mathbf{III}^\pm , and \mathbf{IV}^\pm , the best-fitted value of one of the Yukawa couplings is close to 1, while the other is approximately 0.97 (0.95) or -1 (-0.95).
- In $\mathbf{A}^{\pm\pm, \pm\mp}$, the best-fitted values of C_V are very close to 1, with 1σ errors of about 4%. The best-fitted values of the normalized Yukawa coupling are about 2σ below the SM value of 1, with upper 1σ errors of about 3%–5% when they are positive. When negative, they are around -0.9 , with 1σ errors of 4%–8%.
- The loop-induced coupling ΔS^γ , arising from triangle loops involving the charged Higgs bosons, is generally consistent with the SM in \mathbf{I} , \mathbf{II}^+ ($s_\gamma < 0$), and $\mathbf{A}^{\pm\pm, \pm\mp}$ with 1σ errors of about 0.2. In other cases, ΔS^γ is about 2σ below the SM value of 0, with 1σ errors of around 0.2. For $\Delta S^{Z\gamma}$, we note that the relation $\Delta S^{Z\gamma} \simeq 5 \Delta S^\gamma$ holds, as seen in Eq. (13).

IV. DISCUSSION

In this Section, we provide a detailed description of the results from our global fits of the 2HDMs in the scenarios \mathbf{Inrt} , \mathbf{I} , \mathbf{II}^\pm , and \mathbf{A}^{++} . For the other scenarios, we refer to Appendix A.

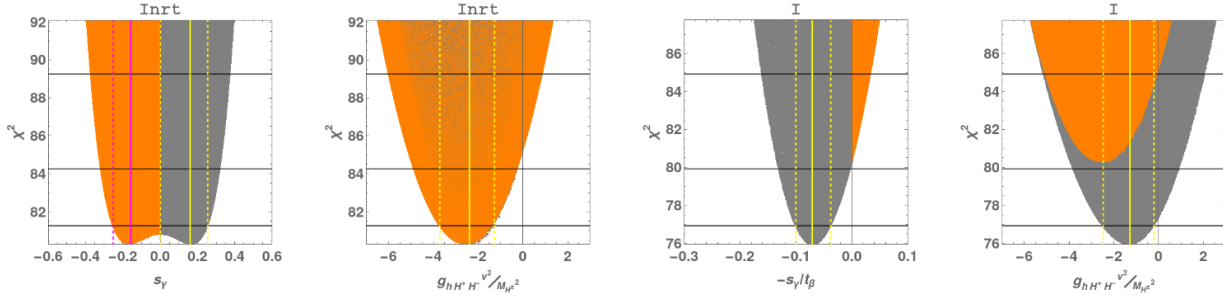


FIG. 2. \mathbf{Inrt} [Two Left] and \mathbf{I} [Two Right]: χ^2 above the minimum versus, from left to right, $-s_\gamma$, $g_{hH^+H^-}(v^2/M_{H^\pm}^2)$, $-s_\gamma/t_\beta$, and $g_{hH^+H^-}(v^2/M_{H^\pm}^2)$ with the orange and gray shaded regions for $s_\gamma < 0$ and $s_\gamma > 0$, respectively. The horizontal lines correspond to $\Delta\chi^2 = 1, 4, 9$, while the magenta and yellow vertical lines indicate the minima and the 1σ CIs for $s_\gamma < 0$ and $s_\gamma > 0$, respectively.

In the two left frames of Fig. 2, we show χ^2 above the minimum as a function of s_γ and the combination $g_{hH^+H^-}(v^2/M_{H^\pm}^2)$ in the \mathbf{Inrt} scenario. Note that, in the frame for χ^2 versus $g_{hH^+H^-}(v^2/M_{H^\pm}^2)$, the orange ($s_\gamma < 0$) and gray ($s_\gamma > 0$) shaded regions completely overlap. We obtain $\chi_{\min}^2/\text{dof} = 80.28/74$ and $\text{gof} = 0.2889$. Two degenerate minima are found around $s_\gamma = \pm 0.2$, with the 1σ CIs of $[-0.25, 0]$ for $s_\gamma < 0$ and $[0, 0.25]$ for $s_\gamma > 0$, which leads to $C_{Vf} = 0.9872^{+0.0128}_{-0.0198}$. For $g_{hH^+H^-}(v^2/M_{H^\pm}^2)$, the minimum occurs around -2.5 , with the 1σ CI of $[-3.7, -1.3]$, independent of the sign of s_γ . This results in $\Delta S^\gamma = -0.421^{+0.180}_{-0.200}$ and $\Delta S^{Z\gamma} = -2.100^{+0.938}_{-0.910} \simeq 5 \Delta S^\gamma$. Note that, for \mathbf{Inrt} , it is not possible to determine the sign of s_γ through Higgs boson precision analysis.

In the two right frames of Fig. 2, we show χ^2 above the minimum as a function of the two novel combinations, $-s_\gamma/t_\beta$ and $g_{hH^+H^-}(v^2/M_{H^\pm}^2)$, in the \mathbf{I} scenario. We obtain $\chi_{\min}^2/\text{dof} = 75.94/73$ and $\text{gof} = 0.3839$. We have obtained the best gof for the \mathbf{I} scenario. The 1σ CIs for the first and second novel combinations are $[-0.10, -0.04]$ and $[-2.5, -0.2]$, respectively, while the 1σ CI for s_γ is $[0, 0.18]$. For the couplings, we find $C_V = 0.9999^{+0.0001}_{-0.0166}$, $C_f^S = 0.929^{+0.033}_{-0.029}$, $\Delta S^\gamma = -0.216^{+0.179}_{-0.200}$ and $\Delta S^{Z\gamma} = -1.036^{+0.859}_{-1.020}$, which are consistent with the 1σ CIs.

⁵Recall that $C_{u,ud,ul}^S = 1 - s_\gamma/t_\beta$ and $C_{d\ell,\ell,d}^S = 1 + s_\gamma t_\beta$.

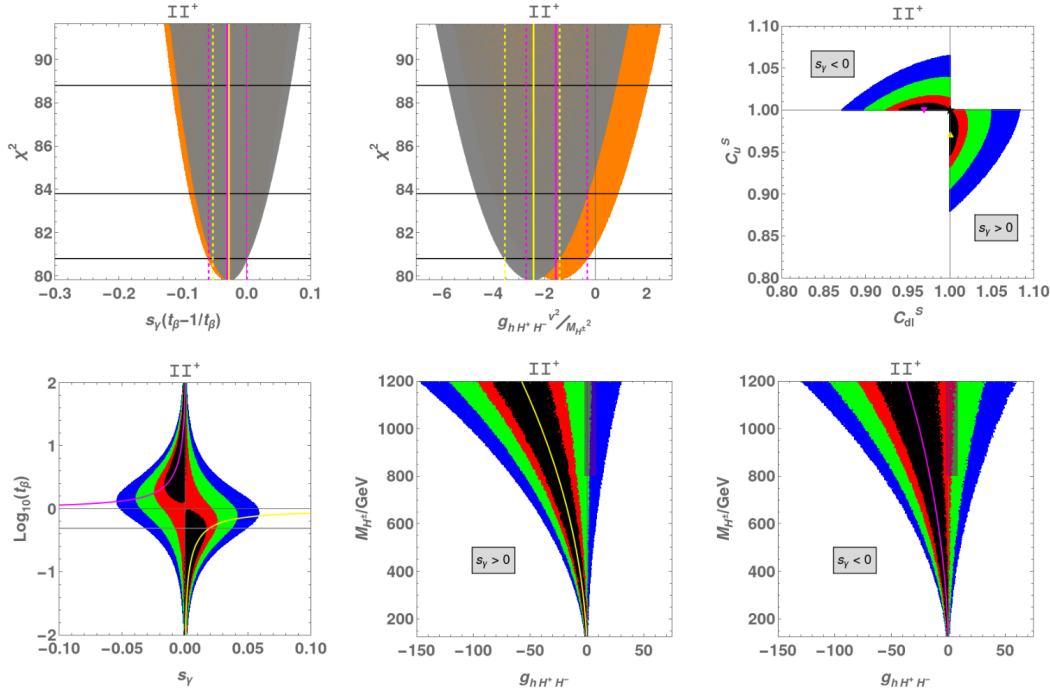


FIG. 3. \mathbf{II}^+ : [Upper] χ^2 above the minimum versus $s_\gamma(t_\beta - 1/t_\beta)$ (left) and $g_{hH^+H^-}(v^2/M_{H^\pm}^2)$ (middle) and the CL regions in the (C_{dl}^S, C_u^S) plane (right). In the left and middle frames, the orange and gray shaded regions represent $s_\gamma < 0$ and $s_\gamma > 0$, respectively. The horizontal lines correspond to $\Delta\chi^2 = 1, 4, 9$, while the magenta and yellow vertical lines indicate the minima and the 1σ CIs for $s_\gamma < 0$ and $s_\gamma > 0$, respectively. [Lower] The CL regions in the $(s_\gamma, \log_{10} t_\beta)$ plane (left) and in the $(g_{hH^+H^-}, M_{H^\pm})$ planes (middle and right). The magenta ($s_\gamma < 0$) and yellow ($s_\gamma > 0$) curves represent the functional relations between the two parameters at the minima given by $s_\gamma(t_\beta - 1/t_\beta) \simeq -0.03$ (left) and $g_{hH^+H^-}(v^2/M_{H^\pm}^2) \simeq -2.5$ (middle; $s_\gamma > 0$), -1.5 (right; $s_\gamma < 0$). In the left frame, the horizontal line denotes the lower limit of $t_\beta > 1/2$, and the lightly shaded narrow regions in the middle and right frames correspond to the constraints of $-2.5 < g_{hH^+H^-} < 8.1$ and $M_{H^\pm} > 800$ GeV. In the upper-right and lower frames, the contour regions represent $\Delta\chi^2 \leq 1$ (black), $\Delta\chi^2 \leq 2.3$ (red), $\Delta\chi^2 \leq 5.99$ (green), $\Delta\chi^2 \leq 11.83$ (blue) above the minimum, which correspond to confidence levels of 39.35%, 68.27%, 95%, and 99.73%, respectively.

In the scenario of \mathbf{II}^+ , in addition to $g_{hH^+H^-}(v^2/M_{H^\pm}^2)$ as in \mathbf{Inrt} and \mathbf{I} , we introduce the following novel combination:

$$s_\gamma \left(t_\beta - \frac{1}{t_\beta} \right), \quad (19)$$

which accounts for the deviation of the normalized Yukawa couplings from the SM value of 1 in the limit $c_\gamma \rightarrow 1$ when t_β is very large or very small. In this limit, either $s_\gamma t_\beta$ or s_γ/t_β remains finite, despite $c_\gamma \rightarrow 1$. We use this same combination of $s_\gamma(t_\beta - 1/t_\beta)$ to analyze the Higgs precision data in \mathbf{III}^+ , as shown in Table II. We find that this combination is useful for addressing the accidental degeneracy in the \mathbf{II}^+ and \mathbf{III}^+ scenarios.

In the upper-left and upper-middle frames of Fig. 3, we show χ^2 above the minimum as a function of the novel combinations for \mathbf{II}^+ . We obtain $\chi_{\min}^2/\text{dof} = 79.82/73$ and $79.85/73$, with $\text{gof} = 0.2734$ and 0.2727 , respectively. For \mathbf{II}^+ , we find two nearly degenerate minima around $s_\gamma(t_\beta - 1/t_\beta) = -0.03$. For example, when $s_\gamma < 0$, $(s_\gamma, t_\beta) \simeq (-0.01, 3)$, and when $s_\gamma > 0$, $(s_\gamma, t_\beta) \simeq (0.01, 1/3)$. This accidental degeneracy is a characteristic feature of the Run 2 LHC Higgs datasets. The two nearly degenerate minima for $s_\gamma(t_\beta - 1/t_\beta)$ are quite close to each other, with a 1σ CI of $[-0.06, 0]$, without distinguishing them. On the other hand, they are slightly separated for $g_{hH^+H^-}(v^2/M_{H^\pm}^2)$, with 1σ CIs of $[-2.7, -0.3]$ for $s_\gamma < 0$ (orange) and $[-3.6, -1.4]$ for $s_\gamma > 0$ (gray). Incidentally, the 1σ CIs for s_γ are $[-0.02, 0]$ for $s_\gamma < 0$ and $[0, 0.02]$ for $s_\gamma > 0$. See Table III for the couplings, which are consistent with the 1σ CIs of s_γ , $s_\gamma(t_\beta - 1/t_\beta)$, and $g_{hH^+H^-}(v^2/M_{H^\pm}^2)$. Note that the two degenerate minima of \mathbf{II}^+ are clearly separated in the (C_u^S, C_{dl}^S) plane. See the upper-right frame of Fig. 3 for the confidence level (CL) regions in the plane, where the two minima are denoted by triangles. Note that both of C_u^S and C_{dl}^S cannot be larger or smaller than 1 simultaneously because $C_u^S = 1 - s_\gamma/t_\beta$ and $C_{dl}^S = 1 + s_\gamma t_\beta$. When $s_\gamma > 0$, the minimum occurs for large t_β , with $s_\gamma(t_\beta - 1/t_\beta) \simeq s_\gamma t_\beta$, and it is located at $(C_u^S, C_{dl}^S) \simeq (0.97, 1)$. When $s_\gamma < 0$, on the other hand, the minimum occurs for small t_β , with $s_\gamma(t_\beta - 1/t_\beta) \simeq -s_\gamma/t_\beta$, and it is located at $(C_u^S, C_{dl}^S) \simeq (1, 0.97)$.

In the three lower frames of Fig. 3, we show the CL regions in the $(s_\gamma, \log_{10} t_\beta)$ and $(g_{hH^+H^-}, M_{H^\pm})$ planes for \mathbf{II}^+ where the magenta ($s_\gamma < 0$) and yellow ($s_\gamma > 0$) curves denote the functional relation between the two parameters at

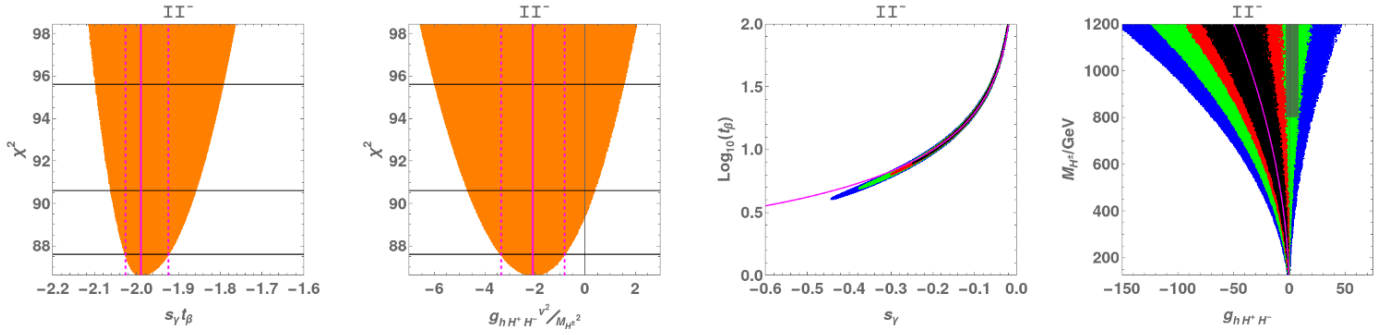


FIG. 4. \mathbf{II}^- : χ^2 above the minimum versus $s_\gamma t_\beta$ and $g_{hH^+H^-}(v^2/M_{H^\pm}^2)$ (two left) and the CL regions in the $(s_\gamma, \log_{10} t_\beta)$ and $(g_{hH^+H^-}, M_{H^\pm})$ planes (two right). The lines, shades, and colors are the same as in Fig. 3.

the minima given by $s_\gamma(t_\beta - 1/t_\beta) \simeq -0.03$ (left) and $g_{hH^+H^-}(v^2/M_{H^\pm}^2) \simeq -2.5$ (middle), -1.5 (right), as seen in the upper-left and upper-middle frames. We observe that the χ^2 behavior of the two novel combinations describes the CL regions in the factored planes quite well.

The alignment parameter $\zeta_u = 1/t_\beta$ cannot be significantly larger than 1 since a large ζ_u (or equivalently, a small t_β) leads to a nonperturbative top-quark Yukawa coupling and a Landau pole near the TeV scale. On the other hand, the analysis of the radiative $b \rightarrow s\gamma$ decay within the type-II and type-IV 2HDMs yields the 95% CL constraint of $M_{H^\pm} > 800$ GeV [18]. In addition, the absolute values of the quartic couplings $Z_{i=1-7}$ cannot be arbitrarily large if the perturbative unitarity (UNIT) conditions and those for the Higgs potential to be bounded from below (BFB) are imposed. By combining the UNIT and BFB conditions with the electroweak (ELW) constraint at 95% CL, the quartic couplings Z_3 and Z_7 are found to be restricted as $-2.4 \lesssim Z_3 \lesssim 8.0$ and $-2.7 \lesssim Z_7 \lesssim 2.7$ [11], which, with $Z_3 = (g_{hH^+H^-} + s_\gamma Z_7)/c_\gamma$, might lead to $-2.5 \lesssim g_{hH^+H^-} \lesssim 8.1$ in \mathbf{II}^+ . In lower frames of Fig. 3, the horizontal line (left) indicates the lower limit of $t_\beta > 1/2$, and the lightly shaded narrow regions (middle and right) represent the constraints of $-2.5 < g_{hH^+H^-} < 8.1$ and $M_{H^\pm} > 800$ GeV. While the constraint of $t_\beta > 1/2$ does not significantly affect the fitting results, we find that when $M_{H^\pm} > 800$ GeV, the allowed region obtained by collectively imposing the UNIT, BFB, and ELW (UBE) constraints lies outside the 68 (39)% CL region for $s_\gamma > 0$ ($s_\gamma < 0$) in the $(g_{hH^+H^-}, M_{H^\pm})$ plane. Note that, if the UBE constraints are imposed for $M_{H^\pm} > 800$ GeV, the degeneracy is lifted, and the minimum occurs when $s_\gamma < 0$. Taking all the constraints into account, we obtain $(\chi_{\min}^2)_{\text{Constrained}}^{\mathbf{II}^+}/\text{dof} = 81.12/73$ and $(\text{gof})_{\text{Constrained}}^{\mathbf{II}^+} = 0.2410$. In this work, we present the unconstrained fitting results, presented in Table III, as our main ones to avoid theoretical biases, while keeping in mind the possibility of the 2HDM framework could be viewed as a low-energy effective field theory like as the SM itself. This approach ensures that the regions of parameter space of phenomenological interest are fully captured without theoretical prejudices or indirect experimental constraints coined from assuming a specific model. Otherwise, see Table IV for the fitting results obtained by imposing $t_\beta > 1/2$ (\mathbf{I} , \mathbf{II}^\pm , \mathbf{III}^\pm , \mathbf{IV}^\pm) or $\zeta_u < 2$ (Aligned), the UBE constraints, and $M_{H^\pm} > 800$ GeV. The last constraint on M_{H^\pm} is applied only in \mathbf{II}^\pm and \mathbf{IV}^\pm .

In the two left frames of Fig. 4, we show χ^2 above the minimum versus the novel combinations for \mathbf{II}^- . We obtain $\chi_{\min}^2/\text{dof} = 86.62/73$ and $\text{gof} = 0.1317$, which represents the worst fit among the 12 scenarios. We note that the minimum occurs around $s_\gamma t_\beta \simeq -2$ when $s_\gamma < 0$ and $t_\beta \gg 1$ with its 1σ CI of $[-2.03, -1.92]$. The 1σ CI for $g_{hH^+H^-}(v^2/M_{H^\pm}^2)$ is $[-3.3, -0.8]$, and for s_γ , it is $[-0.25, -0.02]$. Note that, in this scenario, while $C_{d\ell}^S \simeq -1$ with a 1σ error of 4%, C_u^S is very close to the SM value of 1, with the 1σ errors of less than 0.1%. Compared to \mathbf{II}^+ , the range of s_γ is about 10 times broader, reaching to ~ -0.4 at 95% CL. This is illustrated in the middle-right frame, where the magenta curve denotes the functional relation between s_γ and t_β at the minima, given by $s_\gamma t_\beta \simeq -2$. In the right frame, the magenta curve corresponds to $g_{hH^+H^-}(v^2/M_{H^\pm}^2) \simeq -2$, and the lightly shaded narrow region represents the constraints imposed by the UBE constraints and $M_{H^\pm} > 800$ GeV. When $M_{H^\pm} > 800$ GeV, the UBE allowed region $-3.1 \lesssim g_{hH^+H^-} \lesssim 8.4$ lies just outside the 68% CL region. Under these conditions, we obtain $(\chi_{\min}^2)_{\text{Constrained}}^{\mathbf{II}^-}/\text{dof} = 89.07/73$ and $(\text{gof})_{\text{Constrained}}^{\mathbf{II}^-} = 0.0972$. Note that $s_\gamma > 0$ is completely ruled out in \mathbf{II}^- .

In the upper four frames of Fig. 5, we show χ^2 above the minimum versus the novel combinations of $-s_\gamma \zeta_u$, $-s_\gamma \zeta_d$, $-s_\gamma \zeta_\ell$, and $g_{hH^+H^-}(v^2/M_{H^\pm}^2)$ for \mathbf{A}^{++} . We obtain $\chi_{\min}^2/\text{dof} = 75.67/71$ and $\text{gof} = 0.3302$ constituting the second-best fits together with \mathbf{A}^{+-} , see Fig. 1. For \mathbf{A}^{++} , we find the minima around $-s_\gamma \zeta_u = -0.06$, $-s_\gamma \zeta_d = -0.09$, $-s_\gamma \zeta_\ell = -0.07$, and $g_{hH^+H^-}(v^2/M_{H^\pm}^2) = -1$, with 1σ CIs of $[-0.10, -0.03]$, $[-0.15, -0.04]$, $[-0.12, -0.04]$, and $[-2.13, +0.21]$, respectively. We observe that the positions of the minima and the 1σ CIs match well with the best-fitted values presented in Table III. Notably, the minima occur when $s_\gamma > 0$ (gray shaded regions) and, accordingly, $\zeta_{u,d,\ell} > 0$. In the four lower frames of Fig. 5, we show the CL regions in the $(s_\gamma, \log_{10} \zeta_u)$, $(s_\gamma, \log_{10} |\zeta_d|)$, $(s_\gamma, \log_{10} |\zeta_\ell|)$, and $(g_{hH^+H^-}, M_{H^\pm})$ planes, where the yellow curves denote the functional relation between the two parameters at the minima, given by $s_\gamma \zeta_u \simeq 0.06$, $s_\gamma \zeta_d \simeq 0.09$,

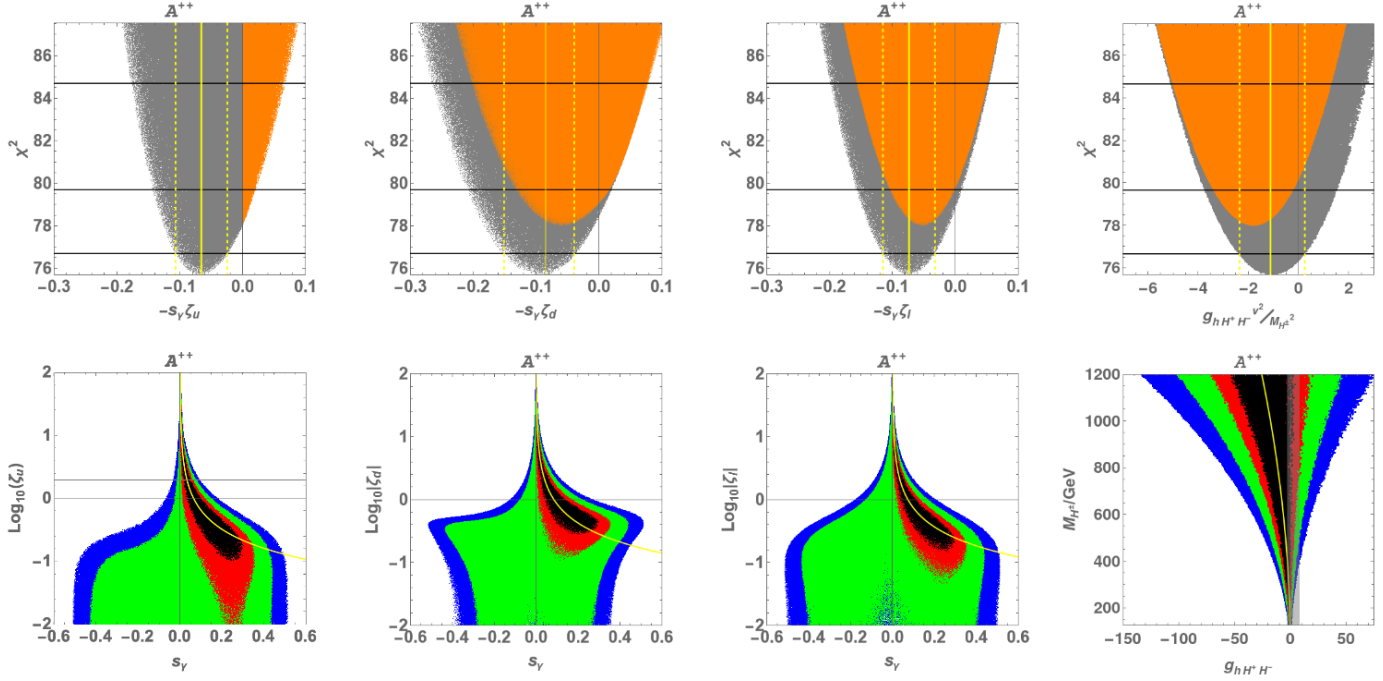


FIG. 5. \mathbf{A}^{++} : [Upper] From left to right, χ^2 above the minimum versus $-s_\gamma\zeta_u$, $-s_\gamma\zeta_d$, $-s_\gamma\zeta_\ell$, and $g_{hH^+H^-}(v^2/M_{H^\pm}^2)$. [Lower] From left to right, the CL regions in the $(s_\gamma, \log_{10}|\zeta_u|)$, $(s_\gamma, \log_{10}|\zeta_d|)$, $(s_\gamma, \log_{10}|\zeta_\ell|)$, and $(g_{hH^+H^-}, M_{H^\pm})$ planes. The lines, shades, and colors are the same as in Fig. 3, but in the lower-left frame, the horizontal line denotes the upper limit of $\zeta_u < 2$.

$s_\gamma\zeta_\ell \simeq 0.07$, and $g_{hH^+H^-}(v^2/M_{H^\pm}^2) \simeq -1$. Once again, we observe that the χ^2 behavior of these four novel combinations adequately describes the CL regions in the factored planes. By imposing $t_\beta > 1/2$, the UBE conditions, and $M_{H^\pm} > 800$ GeV, we obtain $(\chi_{\min}^2)_{\text{Constrained}}^{\mathbf{A}^{++}}/\text{dof} = 75.99/73$ and $(\text{gof})_{\text{Constrained}}^{\mathbf{A}^{++}} = 0.3211$.

We refer to Appendix B for a comprehensive view of the CL regions in the two-coupling planes, showing all possible correlations among the 125 GeV Higgs boson couplings to SM particles in the 12 scenarios of the six types of 2HDMs analyzed in this work.

V. CONCLUSIONS

We perform global fits of 2HDMs to the full Run 1 and Run 2 Higgs datasets collected at the LHC, with the integrated luminosities per experiment of approximately 5 fb^{-1} at 7 TeV, 20 fb^{-1} at 8 TeV [7], and up to 139 fb^{-1} at 13 TeV [3, 4]. For the $H \rightarrow Z\gamma$ signal strength, we use the most recent result obtained in the combined ATLAS and CMS analysis [17]. Requiring the absence of tree-level Higgs-mediated FCNCs, we consider 12 scenarios across six types of 2HDMs: Inert, type I, type II, type III, type IV, and Aligned 2HDMs. The wrong-sign cases are treated as independent scenarios. We assume that the lightest neutral Higgs state plays the role of the 125 GeV Higgs boson discovered at the LHC and focus on its couplings to SM particles. The fitting results are presented in Table III and Fig. 1.

We find that the type-I 2HDM provides the best fit, with $\chi_{\min}^2/\text{dof} = 75.94/73$ and $\text{gof} = 0.3839$, compared to the SM values of $(\chi_{\min}^2/\text{dof})_{\text{SM}} = 85.29/77$ and $(\text{gof})_{\text{SM}} = 0.2424$. In this case, all three normalized Yukawa couplings are identical⁶, with the best-fitted value about 2σ below the SM value of 1, and 1σ errors of 3%. On the other hand, the coupling to the two massive vector bosons saturates to the SM value of 1, with a lower 1σ error of 2%. The loop-induced couplings to $\gamma\gamma$ and $Z\gamma$, when normalized to their corresponding SM values, deviate from the SM value of 0 by about 1σ , with 1σ errors of 3% and 9%, respectively.

We observe that the Aligned 2HDM provides the second-best fit when the Yukawa couplings to down-type quarks take the same sign as in the SM, regardless of the sign of the Yukawa couplings to the charged leptons.⁷ On the other hand, only the wrong-sign scenarios of type-II and type-IV 2HDMs result in worse fits than the SM among the 12 scenarios

⁶In the type-II, type-III, and type-IV 2HDMs, unlike in the type-I 2HDM, the normalized Yukawa coupling to up-type quarks and that to down-type fermions cannot simultaneously be larger or smaller than 1. This explains why these models result in worse fits to the current LHC Higgs datasets.

⁷In fact, we observe slightly better fits when only the Yukawa coupling to the charged leptons has the wrong sign.

considered in this work. Otherwise, the Inert, type-II (with $C_{d\ell}^S > 0$), type-III, type-IV (with $C_d^S > 0$), wrong-sign Aligned (with $C_d^S < 0$) 2HDMs form the third-best fit group.

Last but not least, when the UBE constraints are imposed along with $M_{H^\pm} > 800$ GeV in the type-II and type-IV 2HDMs, we find worse fits than the SM, even when the signs of the Yukawa are the same as in the SM, see Fig. 16.

ACKNOWLEDGMENT

C.B.P. gratefully acknowledges the hospitality at APCTP during the focus program ‘‘Dark Matter as a Portal to New Physics’’ (APCTP-2025-F01). This work was supported by the National Research Foundation (NRF) of Korea Grant No. NRF-2021R1A2B5B02087078 (Y.H., J.S.L.). The work of C.B.P. was supported by the NRF grant funded by the Korea government (Ministry of Science and ICT) (No. RS-2023-00209974). The work was also supported in part by the NRF of Korea Grants No. NRF-2022R1A5A1030700 and No. RS-2024-00442775.

Appendix A: Scenarios of III^\pm , IV^\pm , A^{+-} , A^{-+} , and A^{--}

In this Appendix, we present χ^2 above the minimum versus the novel combinations and the CL regions in the factored two-dimensional planes for the scenarios of III^\pm , IV^\pm , A^{+-} , A^{-+} , and A^{--} , which were not discussed in Sec. IV.

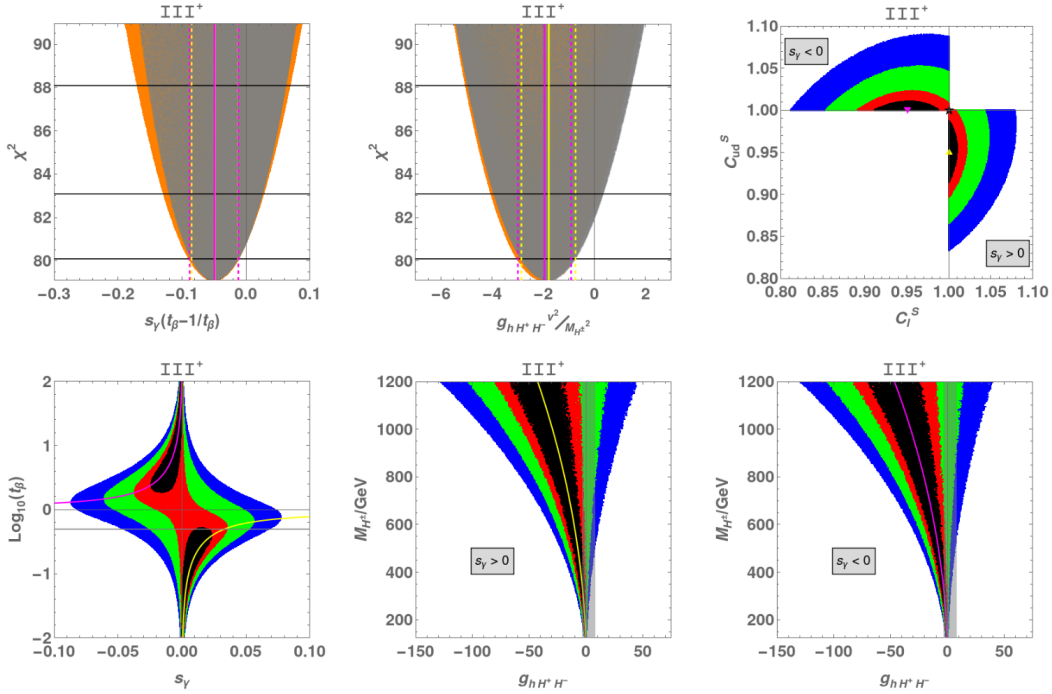


FIG. 6. III^+ : The same as in Fig. 3, but for the III^+ scenario.

Figure 6 shows the results for III^+ , where we observe a two-fold accidental degeneracy depending on the sign of s_γ , as in II^+ and:

- $\chi^2_{\min}/\text{dof} = 79.11/73$ ($79.10/73$) and $\text{gof} = 0.2923$ (0.2923) for $s_\gamma > 0$ ($s_\gamma < 0$)
- Parametric relations at the minima: $s_\gamma(t_\beta - 1/t_\beta) \simeq -0.05$ and $g_{hH^+H^-}(v^2/M_{H^\pm}^2) \simeq -2.0$
- 1σ CIs:
 - $s_\gamma > 0$: $[0, 0.02]$ for s_γ , $[-0.09, -0.01]$ for $s_\gamma(t_\beta - 1/t_\beta)$, and $[-2.9, -0.8]$ for $g_{hH^+H^-}(v^2/M_{H^\pm}^2)$
 - $s_\gamma < 0$: $[-0.02, 0]$ for s_γ , $[-0.09, -0.01]$ for $s_\gamma(t_\beta - 1/t_\beta)$, and $[-3.0, -0.9]$ for $g_{hH^+H^-}(v^2/M_{H^\pm}^2)$
- Characteristic features: The two degenerate minima are clearly separated in the (C_{ud}^S, C_ℓ^S) plane, with the best-fit values of $(C_{ud}^S, C_\ell^S) \simeq (0.95, 1)$ for $s_\gamma > 0$ and $(C_{ud}^S, C_\ell^S) \simeq (1, 0.95)$ for $s_\gamma < 0$

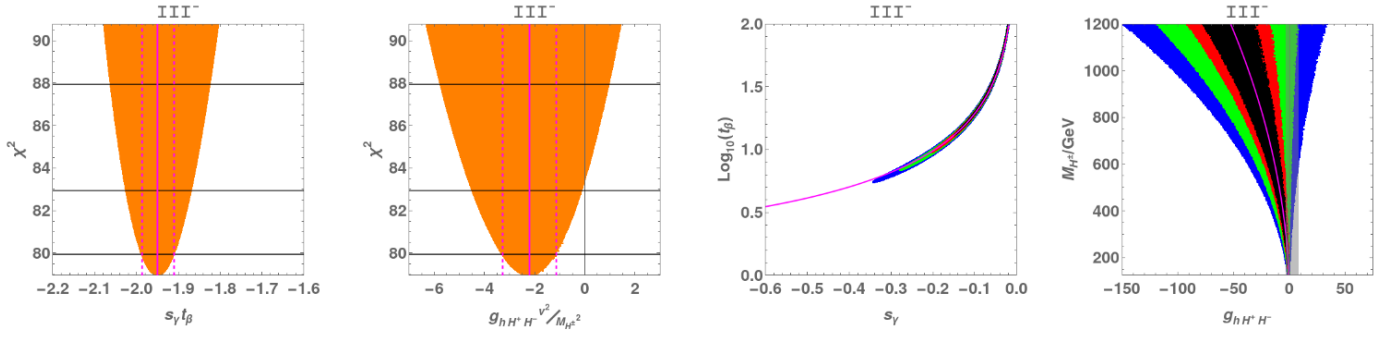


FIG. 7. III^- : The same as in Fig. 4, but for the III^- scenario.

- Imposing $t_\beta > 1/2$ and the UBE conditions: $(\chi_{\min}^2)_{\text{Constrained}}^{\text{III}^+}/\text{dof} = 79.13/73$ and $(\text{gof})_{\text{Constrained}}^{\text{III}^+} = 0.2916$, which are similar to the results without constraints

Figure 7 is for III^- for which we find:

- $\chi_{\min}^2/\text{dof} = 78.96/73$ and $\text{gof} = 0.2962$
- Parametric relations at the minima: $s_\gamma t_\beta \simeq -1.95$ and $g_{hH^+H^-}(v^2/M_{H^\pm}^2) \simeq -2.2$
- 1σ CIs: $[-0.15, -0.02]$ for s_γ , $[-1.99, -1.91]$ for $s_\gamma t_\beta$, and $[-3.3, -1.2]$ for $g_{hH^+H^-}(v^2/M_{H^\pm}^2)$
- Imposing $t_\beta > 1/2$ and the UBE conditions: $(\chi_{\min}^2)_{\text{Constrained}}^{\text{III}^-}/\text{dof} = 78.97/73$ and $(\text{gof})_{\text{Constrained}}^{\text{III}^-} = 0.2961$, which are similar to the results without constraints

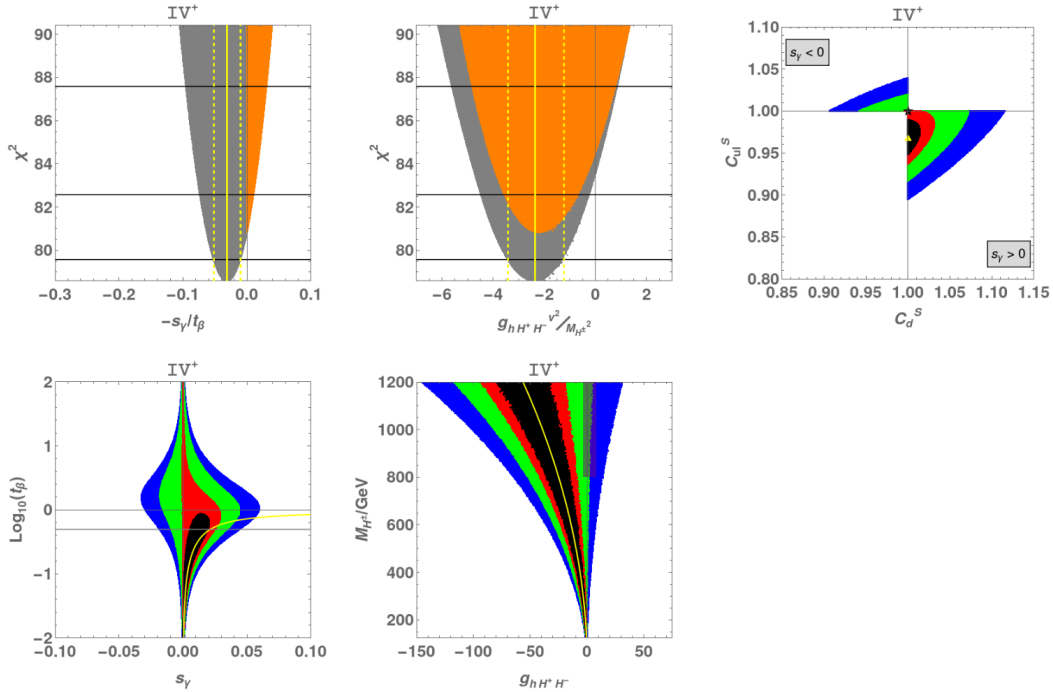


FIG. 8. IV^+ : The same as in Fig. 3, but for the IV^+ scenario.

Figure 8 is for IV^+ for which we find:

- $\chi_{\min}^2/\text{dof} = 78.60/73$ and $\text{gof} = 0.3062$
- Parametric relations at the minima: $-s_\gamma/t_\beta \simeq -0.03$ and $g_{hH^+H^-}(v^2/M_{H^\pm}^2) \simeq -2.4$
- 1σ CIs: $[0, 0.02]$ for s_γ , $[-0.05, -0.01]$ for $-s_\gamma/t_\beta$, and $[-3.4, -1.2]$ for $g_{hH^+H^-}(v^2/M_{H^\pm}^2)$

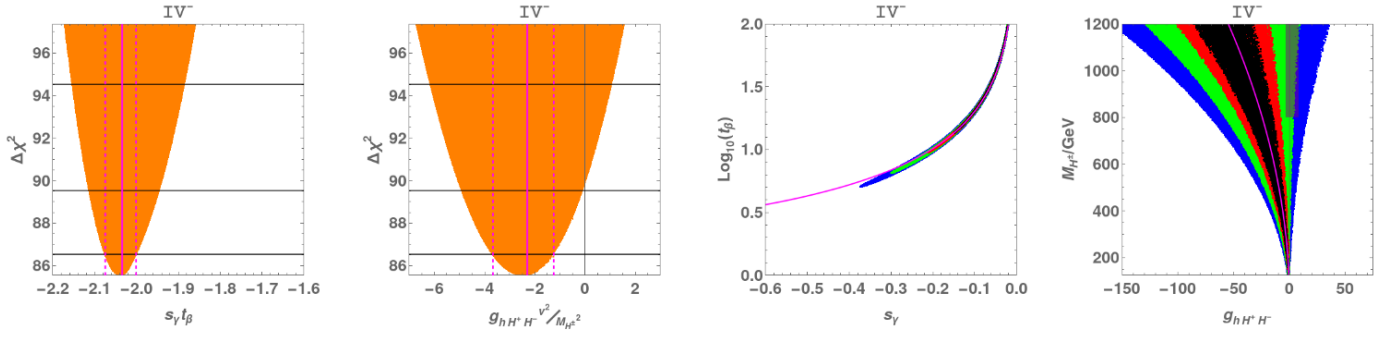


FIG. 9. IV^- : The same as in Fig. 4, but for the IV^- scenario.

- Characteristic features: $s_\gamma > 0$ at 68% CL
- Imposing $t_\beta > 1/2$, the UBE conditions, and $M_{H^\pm} > 800$ GeV: $(\chi^2_{\min})_{\text{Constrained}}^{\text{IV}^+}/\text{dof} = 83.50/73$ and $(\text{gof})_{\text{Constrained}}^{\text{IV}^+} = 0.1880$, which are quite worse compared to the results without constraints

Figure 9 is for IV^- for which we find:

- $\chi^2_{\min}/\text{dof} = 85.55/73$ and $\text{gof} = 0.1495$
- Parametric relations at the minima: $s_\gamma t_\beta \simeq -2.04$ and $g_{hH^+H^-}(v^2/M_{H^\pm}^2) \simeq -2.3$
- 1σ CIs: $[-0.15, -0.02]$ for s_γ , $[-2.08, -2.00]$ for $s_\gamma t_\beta$, and $[-3.7, -1.3]$ for $g_{hH^+H^-}(v^2/M_{H^\pm}^2)$
- Imposing $t_\beta > 1/2$, the UBE conditions, and $M_{H^\pm} > 800$ GeV: $(\chi^2_{\min})_{\text{Constrained}}^{\text{IV}^-}/\text{dof} = 89.35/73$ and $(\text{gof})_{\text{Constrained}}^{\text{IV}^-} = 0.0938$, which are quite worse compared to the results without constraints

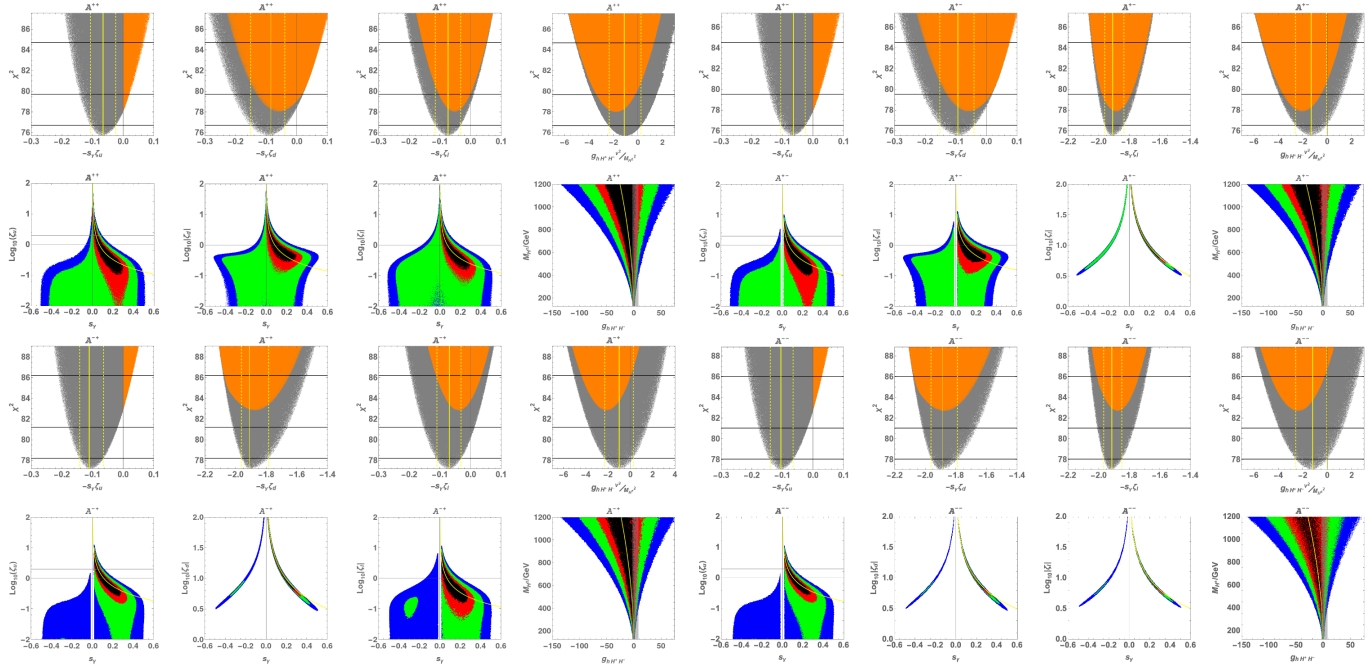


FIG. 10. A^{++} (upper-left), A^{+-} (upper-right), A^{-+} (lower-left), and A^{--} (lower-right). The upper-left panel for A^{++} is the same as Fig. 5 and the lines, shades, and colors are the same as in Fig. 3.

The four panels in Fig. 10 correspond to the four Aligned 2HDM scenarios of A^{++} (upper-left), A^{+-} (upper-right), A^{-+} (lower-left), and A^{--} (lower-right) with each panel containing 8 frames. Note that the upper-left panel for A^{++} is the same as Fig. 5, and we include it again for comparison purposes. Our findings are:

- $\chi^2_{\min}/\text{dof} = 75.70/71$ (A^{++}), $75.52/71$ (A^{+-}), $77.20/71$ (A^{-+}), and $77.03/71$ (A^{--})

- $\text{gof} = 0.3302 (\mathbf{A}^{++}), 0.3347 (\mathbf{A}^{+-}), 0.2873 (\mathbf{A}^{-+}), \text{ and } 0.2918 (\mathbf{A}^{--})$
- Parametric relations at the minima
 - \mathbf{A}^{++} : $-s_\gamma \zeta_u \simeq -0.07$, $-s_\gamma \zeta_d \simeq -0.09$, $-s_\gamma \zeta_\ell \simeq -0.07$, and $g_{h_{H^+H^-}}(v^2/M_{H^\pm}^2) \simeq -1.1$
 - \mathbf{A}^{+-} : $-s_\gamma \zeta_u \simeq -0.06$, $-s_\gamma \zeta_d \simeq -0.09$, $-s_\gamma \zeta_\ell \simeq -1.91$, and $g_{h_{H^+H^-}}(v^2/M_{H^\pm}^2) \simeq -1.3$
 - \mathbf{A}^{-+} : $-s_\gamma \zeta_u \simeq -0.11$, $-s_\gamma \zeta_d \simeq -1.91$, $-s_\gamma \zeta_\ell \simeq -0.07$, and $g_{h_{H^+H^-}}(v^2/M_{H^\pm}^2) \simeq -1.0$
 - \mathbf{A}^{--} : $-s_\gamma \zeta_u \simeq -0.11$, $-s_\gamma \zeta_d \simeq -1.89$, $-s_\gamma \zeta_\ell \simeq -1.91$, and $g_{h_{H^+H^-}}(v^2/M_{H^\pm}^2) \simeq -1.2$
- 1σ CIs:
 - s_γ : $[0, 0.30] (\mathbf{A}^{++})$, $[0.02, 0.30] (\mathbf{A}^{+-})$, $[0.02, 0.28] (\mathbf{A}^{-+})$, and $[0.02, 0.28] (\mathbf{A}^{--})$
 - $-s_\gamma \zeta_u$: $[-0.11, -0.03] (\mathbf{A}^{++})$, $[-0.11, -0.03] (\mathbf{A}^{+-})$, $[-0.14, -0.06] (\mathbf{A}^{-+})$, and $[-0.14, -0.07] (\mathbf{A}^{--})$
 - $-s_\gamma \zeta_d$: $[-0.15, -0.04] (\mathbf{A}^{++})$, $[-0.15, -0.04] (\mathbf{A}^{+-})$, $[-1.96, -1.79] (\mathbf{A}^{-+})$, and $[-1.96, -1.79] (\mathbf{A}^{--})$
 - $-s_\gamma \zeta_\ell$: $[-0.12, -0.03] (\mathbf{A}^{++})$, $[-1.96, -1.84] (\mathbf{A}^{+-})$, $[-0.11, -0.03] (\mathbf{A}^{-+})$, and $[-1.97, -1.85] (\mathbf{A}^{--})$
 - $g_{h_{H^+H^-}}(v^2/M_{H^\pm}^2)$: $[-2.4, 0.2] (\mathbf{A}^{++})$, $[-2.6, -0] (\mathbf{A}^{+-})$, $[-2.3, 0.3] (\mathbf{A}^{-+})$, and $[-2.6, -0] (\mathbf{A}^{--})$
- Characteristic features: In the wrong-sign scenarios of $\mathbf{A}^{+-}, -^{+-}, --$, the region of $|s_\gamma| \lesssim 0.02$ is not accessible. This is because the alignment parameters of $|\zeta_{d,\ell}|$ are scanned up to 100, while $-s_\gamma \zeta_{d,\ell} \simeq -2$ is required
- Imposing $\zeta_u < 2$ and the UBE conditions: ⁸
 - $(\chi_{\min}^2/\text{dof})_{\text{Constrained}}$: $75.99/71 (\mathbf{A}^{++})$, $75.57/71 (\mathbf{A}^{+-})$, $77.32/71 (\mathbf{A}^{-+})$, and $77.12/71 (\mathbf{A}^{--})$
 - $(\text{gof})_{\text{Constrained}}$: $0.3211 (\mathbf{A}^{++})$, $0.3331 (\mathbf{A}^{+-})$, $0.2841 (\mathbf{A}^{-+})$, and $0.2894 (\mathbf{A}^{--})$

Appendix B: Correlations among couplings

In this Appendix, we present the CL regions in the two-coupling planes to illustrate the correlations among the 125 GeV Higgs boson couplings to SM particles in the 12 scenarios of the six types of 2HDMs considered in this work.

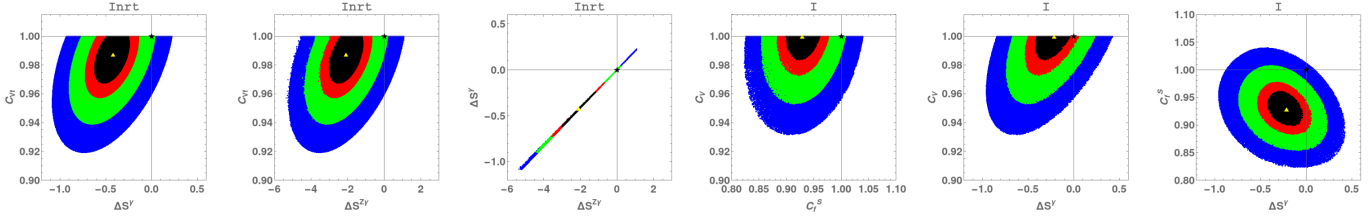


FIG. 11. The CL regions of **Inrt** [Left] and **I** [Right]: In the left panel, we show the CL regions of **Inrt** in the $(\Delta S^\gamma, C_{Vf})$, $(\Delta S^{Z\gamma}, C_{Vf})$, and $(\Delta S^{Z\gamma}, \Delta S^\gamma)$ planes. In the right panel, we show the CL regions of **I** in the (C_f^S, C_V) , $(\Delta S^\gamma, C_V)$, and $(\Delta S^\gamma, C_f^S)$. The contour regions shown are for $\Delta\chi^2 \leq 1$ (black), $\Delta\chi^2 \leq 2.3$ (red), $\Delta\chi^2 \leq 5.99$ (green), $\Delta\chi^2 \leq 11.83$ (blue) above the minimum, which correspond to confidence levels of 39.35%, 68.27%, 95%, and 99.73%, respectively. In each frame, the vertical and horizontal lines indicate the SM point, denoted by a star, while the best-fit point is marked by a triangle.

We highlight the following key points regarding the correlations in the two-dimensional planes of the Higgs couplings:

- **Inrt**: In the left panel of Fig. 11, the CL regions of **Inrt** in the $(\Delta S^\gamma, C_{Vf})$, $(\Delta S^{Z\gamma}, C_{Vf})$, and $(\Delta S^{Z\gamma}, \Delta S^\gamma)$ planes are shown. We observe that the correlation between C_{Vf} and $\Delta S^{Z\gamma}$ (middle) can be easily inferred from the correlation between C_{Vf} and ΔS^γ (left), following the relation $\Delta S^{Z\gamma} \simeq 5\Delta S^\gamma$, as clearly shown in the right frame in the $(\Delta S^{Z\gamma}, \Delta S^\gamma)$ plane. In the remaining scenarios from now on, therefore, we drop the correlations involved with $\Delta S^{Z\gamma}$, as they can be easily deduced from those with ΔS^γ .
- **I** (Right panel of Fig. 11): In this best-fit scenario, the SM point lies outside the 95% CL region in the $(\Delta S^\gamma, C_f^S)$ plane, as shown in the right frame.

⁸See Table IV.

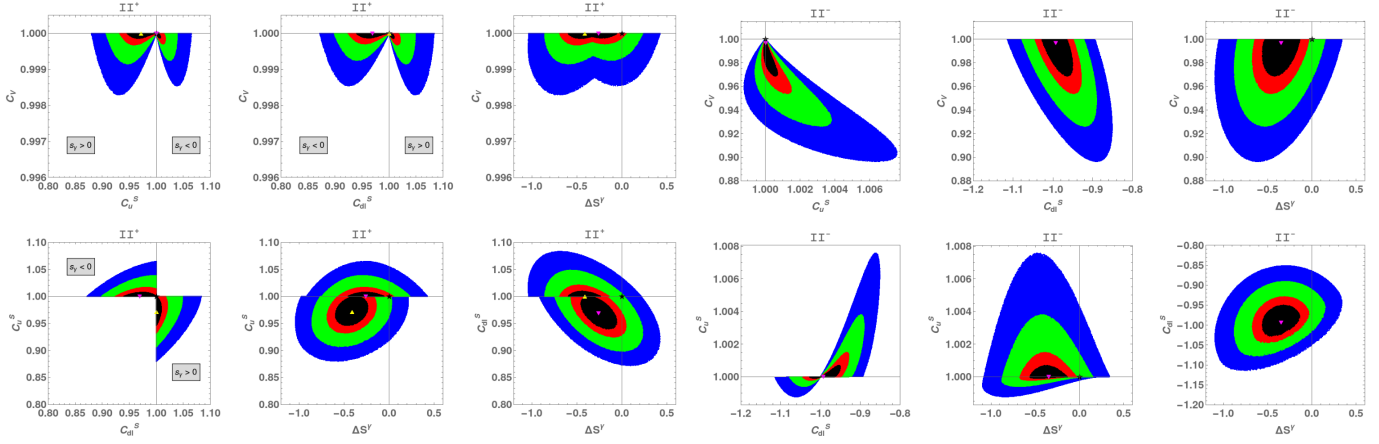


FIG. 12. The CL regions of II^+ [Left] and II^- [Right]: In each panel, the CL regions are shown in the (C_u^S, C_V) (upper-left), (C_d^S, C_V) (upper-middle), $(\Delta S^\gamma, C_V)$ (upper-right), (C_d^S, C_u^S) (lower-left), $(\Delta S^\gamma, C_u^S)$ (lower-middle), and $(\Delta S^\gamma, C_d^S)$ (lower-middle) planes. The lines, colors, and markers are the same as in Fig. 11.

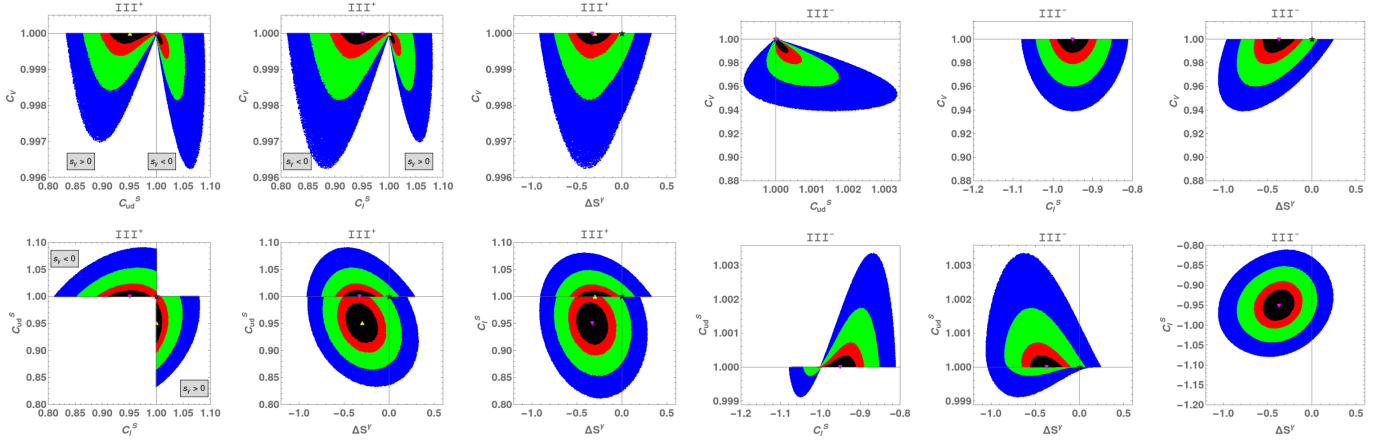


FIG. 13. The CL regions of III^+ [Left] and III^- [Right]: In each panel, the CL regions are shown in the (C_u^S, C_V) (upper-left), (C_l^S, C_V) (upper-middle), $(\Delta S^\gamma, C_V)$ (upper-right), (C_l^S, C_u^S) (lower-left), $(\Delta S^\gamma, C_u^S)$ (lower-middle), and $(\Delta S^\gamma, C_l^S)$ (lower-middle) planes. The lines, colors, and markers are the same as in Fig. 11.

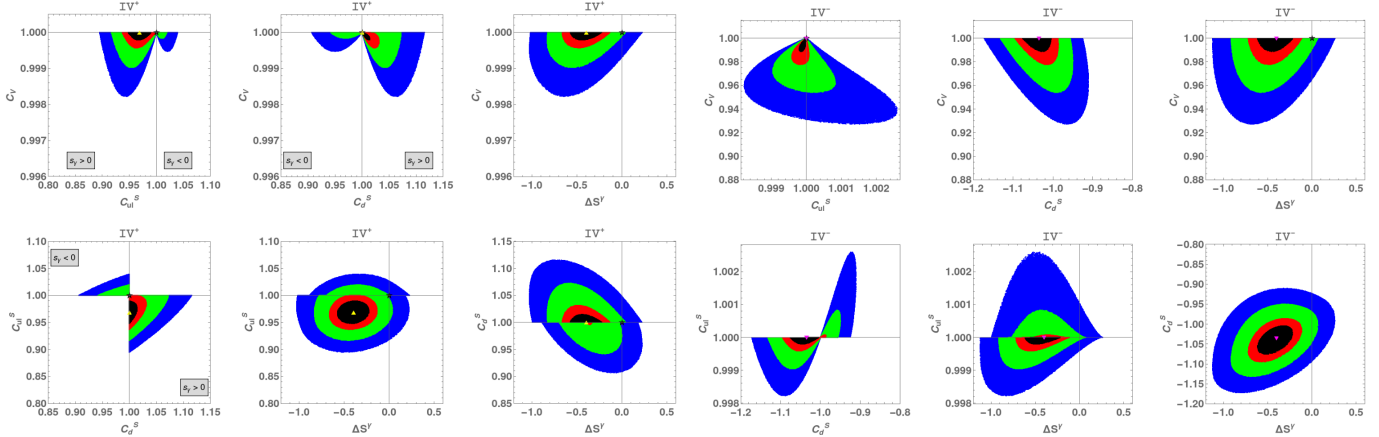


FIG. 14. The CL regions of IV^+ [Left] and IV^- [Right]: In each panel, the CL regions are shown in the (C_u^S, C_V) (upper-left), (C_d^S, C_V) (upper-middle), $(\Delta S^\gamma, C_V)$ (upper-right), (C_d^S, C_u^S) (lower-left), $(\Delta S^\gamma, C_u^S)$ (lower-middle), and $(\Delta S^\gamma, C_d^S)$ (lower-middle) planes. The lines, colors, and markers are the same as in Fig. 11.

- II^+ (Left panel of Fig. 12): The lower-left frame is the same as the upper-right one in Fig. 3. The two separate CL regions, depending $\text{sign}(s_\gamma)$ (also appearing in the upper-left and upper-middle frames), might essentially explain

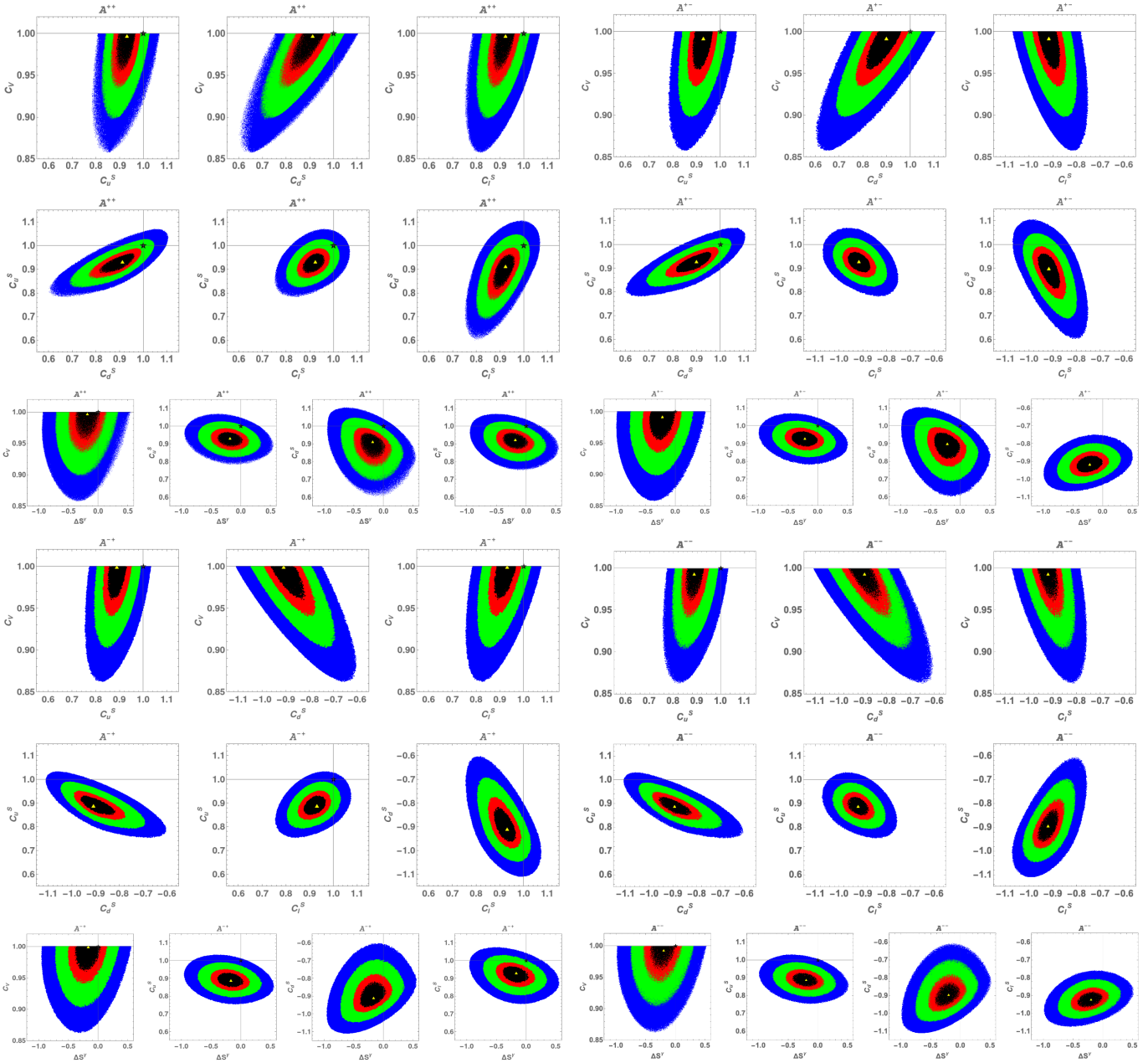


FIG. 15. The CL regions of \mathbf{A}^{++} [Upper-Left], \mathbf{A}^{+-} [Upper-Right], \mathbf{A}^{-+} [Lower-Left], and \mathbf{A}^{--} [Lower-Right]: In each panel, the CL regions are shown in the (C_d^S, C_v) (upper-left), (C_d^S, C_v) (upper-middle), (C_d^S, C_v) (upper-right), (C_d^S, C_u) (middle-left), (C_d^S, C_u) (middle-middle), (C_d^S, C_u) (middle-right), $(\Delta S^\gamma, C_v)$ (lower-left), $(\Delta S^\gamma, C_u)$ (lower-middle-left), $(\Delta S^\gamma, C_d)$ (lower-middle-right), $(\Delta S^\gamma, C_l)$ (lower-right) planes. The lines, colors, and markers are the same as in Fig. 11.

the discontinuities seen in the lower-middle and lower-right frames. The SM point locates at the boundary between the 68% and 95% CL regions in the $(\Delta S^\gamma, C_{dl}^S)$ plane, as shown in the lower-right frame. Note that the two degenerate minima are marked by the yellow ($s_\gamma > 0$) and magenta ($s_\gamma < 0$) triangles.

- \mathbf{II}^- (Right panel of Fig. 12): The deviation of C_u^S from 1 is below 1% at 99.7% CL.
- \mathbf{III}^+ (Left panel of Fig. 13): The lower-left frame is the same as the upper-right one in Fig. 6, and the similar observations to those made in \mathbf{II}^+ can be applied here.
- \mathbf{III}^- (Right panel of Fig. 13): The deviation of C_{ud}^S from 1 is below 0.4% at 99.7% CL.
- \mathbf{IV}^+ (Left panel of Fig. 14): The SM points locate at the boundary between the 68% and 95% CL regions in the $(\Delta S^\gamma, C_v)$ and $(\Delta S^\gamma, C_d^S)$ planes, as shown in the upper-right and lower-right frames.

- **IV⁻** (Right panel of Fig. 14): The deviation of $C_{u\ell}^S$ from 1 is below 0.3% at 99.7% CL.
- **A⁺⁺** (Upper-Left panel of Fig. 15): The 68% CL regions (and most of 95% CL regions) lie where all of the Yukawa couplings are smaller than 1, as shown in the three middle frames. This is consistent with our finding that the type-I 2HDM gives the best fit. The SM points locate at the boundary between the 68% and 95% CL regions in the $(\Delta S^\gamma, C_u^S)$, $(\Delta S^\gamma, C_d^S)$, and $(\Delta S^\gamma, C_\ell^S)$ planes, as shown in the lower frames.
- **A^{++,+-,-+,-}** (Fig. 15): We find a stronger correlation between C_V and C_d^S than between C_V and $C_{u\ell}^S$, as seen in the upper frames in each panel. Again in these upper frames, we observe that the correlation between C_V and C_d^S flips its sign under **A⁺⁺** \leftrightarrow **A⁻⁺⁺**, while that between C_V and C_ℓ^S under **A⁺⁺** \leftrightarrow **A⁻⁺⁺**. Similar sign flips of the correlations are observed across the panels.

Appendix C: Constrained fitting results

TABLE IV. The minimal chi-square per degree of freedom (χ_{\min}^2/dof), goodness of fit (gof), 1σ confidence interval of s_γ , the 95% CL region of $g_{hH^+H^-}$, and the best-fitted values of the 125 GeV Higgs couplings to SM particles in the 12 scenarios considered in our global fit to the six types of 2HDMs. Imposed are the constraints from: the UBE conditions for **Inrt**; $t_\beta > 1/2$ and the UBE conditions for **I** and **III[±]**; $t_\beta > 1/2$, the UBE conditions, and $M_{H^\pm} > 800$ GeV for **II[±]** and **IV[±]**; and $\zeta_u < 2$ and the UBE conditions for **A^{±±,±∓}**. For the SM, we obtain $\chi_{\min}^2/\text{dof} = 85.29/77$ and $\text{gof} = 0.2424$.

		χ^2_{\min}/dof	gof	s_γ	$g_{hH^+H^-}$	C_V	C_f^S			ΔS^γ	$\Delta S^{Z\gamma}$
Inrt	$s_\gamma > 0$	80.28/74	0.2889	[0, 0.25]	[-3.2, 8.4]	$C_{Vf} = 0.9872^{+0.0128}_{-0.0198}$			$-0.421^{+0.180}_{-0.194}$	$-2.100^{+0.926}_{-0.910}$	
	$s_\gamma < 0$			[-0.25, 0]							
I		76.03/73	0.3810	[0.03, 0.19]	[-3.0, 8.3]	$0.9967^{+0.0030}_{-0.0143}$	$0.928^{+0.031}_{-0.027}$			$-0.231^{+0.193}_{-0.191}$	$-1.119^{+0.938}_{-0.956}$
II ⁺		81.12/73	0.2410	[-0.02, 0]	[-2.5, 8.1]	$1.0_{-0.0001}$	$C_u^S = 1.0^{+0.006}_{-0.000}$	$C_{d\ell}^S = 0.950^{+0.027}_{-0.022}$	$-0.031^{+0.079}_{-0.006}$	$-0.149^{+0.380}_{-0.030}$	
II ⁻		89.07/73	0.0972	[-0.19, -0.02]	[-3.1, 8.4]	$0.9988^{+0.0010}_{-0.0170}$	$C_u^S = 1.0^{+0.001}_{-0.000}$	$C_{d\ell}^S = -0.975^{+0.033}_{-0.020}$	$-0.026^{+0.062}_{-0.014}$	$-0.126^{+0.297}_{-0.066}$	
III ⁺		79.13/73	0.2916	[-0.02, 0]	[-2.5, 8.1]	$1.0_{-0.0003}$	$C_{ud}^S = 1.0^{+0.010}_{-0.000}$	$C_\ell^S = 0.944^{+0.039}_{-0.029}$	$-0.303^{+0.150}_{-0.185}$	$-1.487^{+0.747}_{-0.909}$	
III ⁻		78.97/73	0.2961	[-0.14, -0.02]	[-3.0, 8.3]	$0.9997^{+0.0001}_{-0.0100}$	$C_{ud}^S = 1.0^{+0.0003}_{-0.000}$	$C_\ell^S = -0.947^{+0.030}_{-0.040}$	$-0.383^{+0.175}_{-0.147}$	$-1.859^{+0.841}_{-0.722}$	
IV ⁺		83.50/73	0.1880	[-0.01, 0.02]	[-2.5, 8.0]	$1.0_{-0.0001}$	$C_{u\ell}^S = 0.982^{+0.020}_{-0.018}$	$C_d^S = 1.004^{+0.007}_{-0.048}$	$-0.031^{+0.038}_{-0.006}$	$-0.148^{+0.181}_{-0.029}$	
IV ⁻		89.35/73	0.0938	[-0.11, -0.02]	[-2.9, 8.3]	$0.9996^{+0.0002}_{-0.0060}$	$C_{u\ell}^S = 1.0^{+0.000}_{-0.0001}$	$C_d^S = -1.007^{+0.027}_{-0.031}$	$-0.029^{+0.047}_{-0.009}$	$-0.138^{+0.226}_{-0.042}$	
							C_u^S	C_d^S	C_ℓ^S		
A ⁺⁺		75.99/71	0.3211	[0.03, 0.27]	[-3.4, 8.4]	$0.9983^{+0.0011}_{-0.0364}$	$0.922^{+0.044}_{-0.032}$	$0.887^{+0.069}_{-0.074}$	$0.911^{+0.045}_{-0.040}$	$-0.074^{+0.141}_{-0.311}$	$-0.355^{+0.680}_{-1.520}$
A ⁺⁻		75.57/71	0.3331	[0.03, 0.27]	[-3.4, 8.4]	$0.9913^{+0.0083}_{-0.0283}$	$0.932^{+0.020}_{-0.045}$	$0.910^{+0.037}_{-0.080}$	$-0.924^{+0.045}_{-0.030}$	$-0.240^{+0.233}_{-0.149}$	$-1.164^{+1.131}_{-0.727}$
A ⁻⁺		77.32/71	0.2841	[0.05, 0.27]	[-3.4, 8.4]	$0.9879^{+0.0111}_{-0.0253}$	$0.890^{+0.032}_{-0.035}$	$-0.887^{+0.063}_{-0.059}$	$0.909^{+0.045}_{-0.034}$	$-0.142^{+0.188}_{-0.245}$	$-0.685^{+0.907}_{-1.198}$
A ⁻⁻		77.12/71	0.2894	[0.05, 0.26]	[-3.4, 8.4]	$0.9968^{+0.0018}_{-0.0309}$	$0.884^{+0.046}_{-0.029}$	$-0.899^{+0.068}_{-0.043}$	$-0.931^{+0.047}_{-0.026}$	$-0.182^{+0.181}_{-0.245}$	$-0.879^{+0.876}_{-1.194}$

In this Appendix, we show the fitting results obtained by imposing the following constraints depending on scenarios:

- **Inrt**: the UBE conditions
- **I** and **III[±]**: $t_\beta > 1/2$ and the UBE conditions
- **II[±]** and **IV[±]**: $t_\beta > 1/2$, the UBE conditions, and $M_{H^\pm} > 800$ GeV [18]
- **A^{±±,±∓}**: $\zeta_u < 2$ and the UBE conditions

In this work, we have not considered other constraints, such as those from flavor observables other than the radiative $b \rightarrow s\gamma$ decay or direct searches for heavy scalars at the LHC. This is because we concentrate on the 125 GeV Higgs couplings to SM particles, without specifying the detailed properties of the heavier Higgs states.

In Table IV and Fig. 16, we present the fitting results obtained by imposing the constraints outlined above. While two degenerate minima remain indistinguishable in **Inrt**, the accidental degeneracies in **II⁺** and **III⁺** are lifted. Overall, we observe that the constraints from $t_\beta > 1/2$ (or $\zeta_u < 2$) and the UBE conditions have little effect on the fitting results by themselves. However, when the UBE conditions are combined with $M_{H^\pm} > 800$ GeV, as in the cases of **II[±]** and **IV[±]**, the fits become significantly worse. This is obviously because $\Delta S^{Z\gamma}/5 \simeq \Delta S^\gamma \simeq g_{hH^+H^-}(v^2/M_{H^\pm}^2)/6$ cannot deviate from the SM value of 0 when the two constraints are simultaneously imposed and one fails to accommodate the LHC data $\mu(\sum \mathcal{P}, \gamma\gamma) = 1.10 \pm 0.07$ [5] and $\hat{\mu}^{\text{EXP}}(Z\gamma) = 2.2 \pm 0.7$ [17] comfortably. Now we have the worse gof values than the SM in **II[±]** and **IV[±]**. Otherwise, we again find that scenario **I** provides the best fit. The wrong-sign C_d^S leads to the worse fits in **A^{-±}** compared to **A^{+±}**. Additionally, the wrong-sign scenarios of **III⁻**, **A⁺⁻**, and **A⁻⁻**, with $C_\ell^S < 0$, result in the better fits than the corresponding ones with $C_\ell^S > 0$, though the difference is slight.

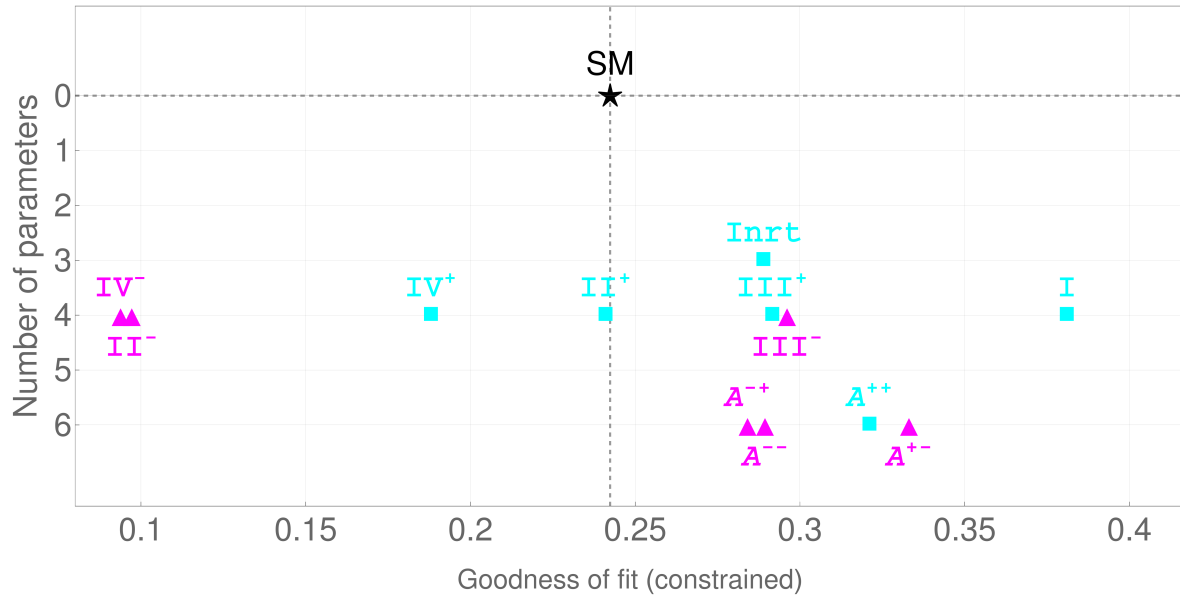


FIG. 16. The same as in Fig. 1, but imposing the constraints from: the UBE conditions for **Inrt**; $t_\beta > 1/2$ and the UBE conditions for **I** and **III** $^\pm$; $t_\beta > 1/2$, the UBE conditions, and $M_{H^\pm} > 800$ GeV for **II** $^\pm$ and **IV** $^\pm$; and $\zeta_u < 2$ and the UBE conditions for **A** $^{\pm\pm,\pm\mp}$.

For the couplings, we observe similar behavior to the unconstrained cases, except for ΔS^γ and $\Delta S^{Z\gamma}$ in **II** $^\pm$ and **IV** $^\pm$, which are significantly reduced by imposing the UBE constraints and $M_{H^\pm} > 800$ GeV. Note that we also provide the 95% CL region of $g_{hH^+H^-}$ in Table IV.

-
- [1] G. Aad *et al.* [ATLAS], “Observation of a new particle in the search for the Standard Model Higgs boson with the ATLAS detector at the LHC,” Phys. Lett. B **716**, 1-29 (2012) doi:10.1016/j.physletb.2012.08.020 [arXiv:1207.7214 [hep-ex]].
 - [2] S. Chatrchyan *et al.* [CMS], “Observation of a New Boson at a Mass of 125 GeV with the CMS Experiment at the LHC,” Phys. Lett. B **716**, 30-61 (2012) doi:10.1016/j.physletb.2012.08.021 [arXiv:1207.7235 [hep-ex]].
 - [3] [ATLAS], “A detailed map of Higgs boson interactions by the ATLAS experiment ten years after the discovery,” Nature **607** (2022) no.7917, 52-59 [erratum: Nature **612** (2022) no.7941, E24] doi:10.1038/s41586-022-04893-w [arXiv:2207.00092 [hep-ex]].
 - [4] A. Tumasyan *et al.* [CMS], “A portrait of the Higgs boson by the CMS experiment ten years after the discovery,” Nature **607** (2022) no.7917, 60-68 doi:10.1038/s41586-022-04892-x [arXiv:2207.00043 [hep-ex]].
 - [5] Y. Heo, D. W. Jung and J. S. Lee, “Higgs boson precision analysis of the full LHC run 1 and run 2 data,” Phys. Rev. D **110**, no.1, 013003 (2024) doi:10.1103/PhysRevD.110.013003 [arXiv:2402.02822 [hep-ph]].
 - [6] T. Biekötter and M. Pierre, “Higgs-boson visible and invisible constraints on hidden sectors,” Eur. Phys. J. C **82**, no.11, 1026 (2022) doi:10.1140/epjc/s10052-022-10990-x [arXiv:2208.05505 [hep-ph]].
 - [7] G. Aad *et al.* [ATLAS and CMS], “Measurements of the Higgs boson production and decay rates and constraints on its couplings from a combined ATLAS and CMS analysis of the LHC pp collision data at $\sqrt{s} = 7$ and 8 TeV,” JHEP **08**, 045 (2016) doi:10.1007/JHEP08(2016)045 [arXiv:1606.02266 [hep-ex]].
 - [8] G. C. Branco, P. M. Ferreira, L. Lavoura, M. N. Rebelo, M. Sher and J. P. Silva, “Theory and phenomenology of two-Higgs-doublet models,” Phys. Rept. **516**, 1-102 (2012) doi:10.1016/j.physrep.2012.02.002 [arXiv:1106.0034 [hep-ph]].
 - [9] A. Pich and P. Tuzon, “Yukawa Alignment in the Two-Higgs-Doublet Model,” Phys. Rev. D **80** (2009), 091702 doi:10.1103/PhysRevD.80.091702 [arXiv:0908.1554 [hep-ph]].
 - [10] S. L. Glashow and S. Weinberg, “Natural Conservation Laws for Neutral Currents,” Phys. Rev. D **15** (1977) 1958.
 - [11] J. S. Lee and J. Park, “Yukawa alignment revisited in the Higgs basis,” Phys. Rev. D **106**, no.1, 015023 (2022) doi:10.1103/PhysRevD.106.015023 [arXiv:2110.03908 [hep-ph]].
 - [12] J. F. Donoghue and L. F. Li, “Properties of Charged Higgs Bosons,” Phys. Rev. D **19** (1979), 945 doi:10.1103/PhysRevD.19.945
 - [13] H. Georgi and D. V. Nanopoulos, “Suppression of Flavor Changing Effects From Neutral Spinless Meson Exchange in Gauge Theories,” Phys. Lett. B **82** (1979), 95-96 doi:10.1016/0370-2693(79)90433-7
 - [14] S. Y. Choi, J. S. Lee and J. Park, “Decays of Higgs bosons in the Standard Model and beyond,” Prog. Part. Nucl. Phys. **120**, 103880 (2021) doi:10.1016/j.pnpnp.2021.103880 [arXiv:2101.12435 [hep-ph]].
 - [15] A. Juste, in Proceedings of HCP2012, 15 November 2012, Kyoto, Japan, <http://kds.kek.jp/conferenceDisplay.py?confId=9237>.
 - [16] K. Herner [CDF and D0], “Higgs Boson Studies at the Tevatron,” Nucl. Part. Phys. Proc. **273-275**, 852-856 (2016) doi:10.1016/j.nuclphysbps.2015.09.131
 - [17] G. Aad *et al.* [ATLAS and CMS], “Evidence for the Higgs Boson Decay to a Z Boson and a Photon at the LHC,” Phys. Rev. Lett. **132**, 021803 (2024) doi:10.1103/PhysRevLett.132.021803 [arXiv:2309.03501 [hep-ex]].

- [18] M. Misiak, A. Rehman and M. Steinhauser, “Towards $\overline{B} \rightarrow X_s \gamma$ at the NNLO in QCD without interpolation in m_c ,” JHEP **06**, 175 (2020) doi:10.1007/JHEP06(2020)175 [arXiv:2002.01548 [hep-ph]].